Published by IOP Publishing for Sissa Medialab

Received: *October 8, 2024*
Revised: *December 11, 2024*
Accepted: *December 19, 2024*
Published: *January 24, 2025*

A high repetition rate millimeter wavelength accelerator for an X-ray free-electron laser

A. Zholents[a,*] **S. Baturin**[b,c] **S. Doran**[a] **W. Jansma**[a] **M. Fedurin**[d] **M. Kasa**[a] **K. Kusche**[d] **S. Lee**[a,e] **A. Nassiri**[a] **P. Piot**[a,b] **B. Popovic**[a] **M. Qian**[a] **A. Siy**[a,f,g] **S. Sorsher**[a] **K. Suthar**[a] **E. Trakhtenberg**[a] **G. Waldschmidt**[a] **and J. Xu**[a]

[a] *Argonne National Laboratory, Lemont, IL 60439, U.S.A.*
[b] *Department of Physics, Northern Illinois University, DeKalb, IL 60115, U.S.A.*
[c] *School of Physics and Engineering, ITMO University, St. Petersburg 197101, Russia*
[d] *Brookhaven National Laboratory, Upton, NY 11973, U.S.A.*
[e] *Los Alamos National Laboratory, Los Alamos, NM 87545, U.S.A.*
[f] *University of Wisconsin-Madison, Madison, WI 53706, U.S.A.*
[g] *Quaise Energy, Cambridge, MA 02138, U.S.A.*

E-mail: azholents@anl.gov

Abstract: A compact collinear wakefield accelerator has been designed for an X-ray free-electron laser capable of operating at a pulse repetition rate in the tens of kilohertz. The maximum achievable accelerating gradient has been determined, with its limitation linked to beam breakup instability. The fabrication techniques for the principal components of the accelerator including wakefield generation, couplers for excess power extraction and diagnostics, focusing quadrupoles, and a novel undulator have been discussed. Results from various laboratory and beam-based tests on these components have been compared to their original design specifications and demonstrated very good agreement. A preliminary design for the XFEL has been presented, featuring a novel small-period, force-neutral, adjustable-phase undulator.

Keywords: Accelerator Subsystems and Technologies; Wake-field acceleration (laser-driven, electron-driven); Accelerator modelling and simulations (multi-particle dynamics, single-particle dynamics)

*Corresponding author.

https://doi.org/10.1088/1748-0221/20/01/P01023

Contents

1 Preamble

The capability of the X-ray Free-Electron Laser (XFEL) to produce diffraction-limited, and in some cases Fourier-transform-limited, X-ray pulses that are billions of times brighter than the peak X-ray brightness attained by the best synchrotrons has sparked a strong demand from scientists for this cutting-edge research instrument [1–3]. At present, nine XFELs operate [4–12], two upgrades are in consideration [13, 14], and three more XFELs are at the various stages of design studies [15–18]. The upgrades and new constructions aim to address the limited capacity of existing XFELs. Obtaining a high average photon flux is planned by incorporating a superconducting radio frequency linear accelerator (SRF) in the designs. The linac will supply evenly spaced electron bunches that can be directed to a single XFEL undulator at a megahertz-scale repetition rate or be shared at a lower repetition rate between several XFEL undulators, thereby boosting the experiment throughput of the facility. The advent of the high repetition rate XFELs has initiated a paradigm shift in obtaining high-resolution three-dimensional structural information of disordered samples under investigation using coherent diffractive imaging [19, 20] and incoherent diffractive imaging [21], also known as fluorescence intensity correlation imaging [22]. These are photon-hungry experimental techniques. The number of required X-ray shots depends on the desired spatial resolution [23, 24]. For atomic resolution, millions of shots, as suggested in [25, 26], will be required, which could be obtained within approximately 10 minutes of data acquisition at the XFEL operating at 20 kHz.

2025 JINST 20 P01023

Meanwhile, the international accelerator physics community's efforts in developing novel accelerator technologies for the linear collider (see [27–30] and references therein) have paved the way for the construction of compact accelerators for new XFELs utilizing plasma, as acknowledged in the European roadmap for accelerator R&D [31] and several other reports [32–40]. The plasma is used as a medium for the intense laser or electron beams to produce the wakefield to accelerate electrons rapidly. However, adopting this technology to XFELs is a non-trivial task since the electron bunches are created on a tens of micrometers length scale, which is not much different from the plasma wavelength of $\sim 100\,\mu m$. This proximity directly impacts the beam's energy spread and brightness, rendering it unsuitable for lasing in a hard X-ray FEL. The proneness of plasma wakefield accelerators to different jitter sources and beam instabilities undermines the repeatability of beam parameters. While these challenges can be addressed, the realization of the hard X-ray FEL driven by a plasma-based accelerator may require significant R&D. A substantial time may be needed to develop a laser for a high-repetition-rate plasma-based accelerator.

Another novel accelerator technology could have a shorter R&D timeframe to achieve readiness for application to XFELs. It relies on the cryogenically cooled copper RF cavities to get up to four times higher accelerating field than those produced by the state-of-the-art structure-based linear accelerators (see [41, 42] and references therein). This leads to a proportional reduction in the accelerator's footprint. Therefore, this technology was adopted for the design of an ultra-compact XFEL [43]. Additionally, a cryogenically cooled photocathode gun is integrated into the proposal to generate substantially brighter electron beams than the best-performing existing electron guns because of the higher electrical field on a cathode [44]. Consequently, if this brightness can be maintained throughout the acceleration and electron bunch compression linac stages, the length of the XFEL undulator could be significantly reduced, too.

A study reported in [45] opted for the path to a compact XFEL without undertaking extensive R&D by leveraging the latest innovations in X-band linac and undulator technologies.

However, a significant drawback of both projects [43, 45] stems from feeding the normal conducting accelerating structures with long pulses of electromagnetic fields from external RF sources. This necessitates operating accelerators with a low RF pulse repetition rate to prevent overheating of the accelerating structures. Consequently, the XFELs in these projects are constrained to operate at an X-ray pulse repetition rate significantly lower than the megahertz-scale X-ray pulse repetition rate of XFELs driven by continuous wave (cw) superconducting linear accelerators. It is important to note that XFELs operating at a low repetition rate cannot significantly boost the number of photons per pulse to produce the average photon flux comparable to high-repetition-rate XFELs without risking sample destruction.

The two approaches to a compact accelerator discussed so far are united by the structure-based wakefield accelerator (SWFA) concept, which has a long history evidenced by publications [46–51]. Reference [52] contains a brief review of recent projects and future directions. The most mature SWFA design is the design of the accelerator for a Compact Linear Collider (CLIC) [53]. It implements a two-beam accelerator scheme where the drive beam generates RF power in the passive structures of the decelerator [54] that is then efficiently transferred, using a waveguide network, to the parallel accelerator for the main beam acceleration. In each operational cycle, repeating at 50 Hz, 312 electron bunches, with a bunch spacing of 0.5-nanoseconds, undergo acceleration [55]. This accelerator operation is focused on producing a high luminosity and suits CLIC users. The limitations on the repetition rate in operation are imposed by facility power consumption and overheating of the accelerating structures.

2025 JINST 20 P01023

Conversely, XFEL users prefer to expose the sample to a solitary X-ray pulse, capture the data, retain or replace the sample, and repeat the process immediately after that. Therefore, the basic requirement for the accelerator supporting XFEL operation is to accelerate solitary electron bunches separated by the time needed for the data acquisition or sample replacement. A collinear wakefield accelerator (CWA), another variant of the SWFA technology, is well-suited for this operation. The CWA uses one structure to passively decelerate, typically, one high-charge drive bunch and to accelerate one low-charge witness electron bunch following close behind the drive bunch. The structure acts as a slow wave medium in which electrons moving near the speed of light produce Čerenkov radiation. The authors of [56] discovered that the radiation fields of individual electrons can be effectively combined to obtain a significantly larger accelerating wakefield for the witness bunch compared to the decelerating wakefield inside the drive bunch by shaping the electron distribution within the drive bunch. The ratio of these fields is called the transformer ratio.

Since the wakefield in the CWA needs to exist only for a short time, using structures that facilitate the rapid decay of the wakefield is advantageous for reducing impulse heating of the structure by the wakefield and thereby increasing the bunch repetition rate of the CWA. Furthermore, extensive research [57, 58] indicates that using short wakefield pulses can increase the electric field breakdown threshold. Operating the CWA at a sub-terahertz frequency provides such opportunities.

In summary, after a comparative analysis of different options for a compact accelerator, the structure-based collinear wakefield accelerator operating at a sub-terahertz frequency was determined to be most suitable for an XFEL operating with a high repetition rate of X-ray pulses evenly spaced in time. For brevity, we call it A-STAR, an acronym for Argonne Sub-Terahertz Accelerator.

2 Introduction

We consider constructing a compact X-ray facility equipped with up to ten XFELs to maximize facility productivity [59, 60]. The facility schematic is shown in figure 1. Each XFEL will have a designated A-STAR designed to accelerate electron bunches by a wakefield with an amplitude of approximately 90 MV/m from 1 GeV to a maximum energy of 4.5 GeV, operating at a repetition rate of up to 20 kHz.

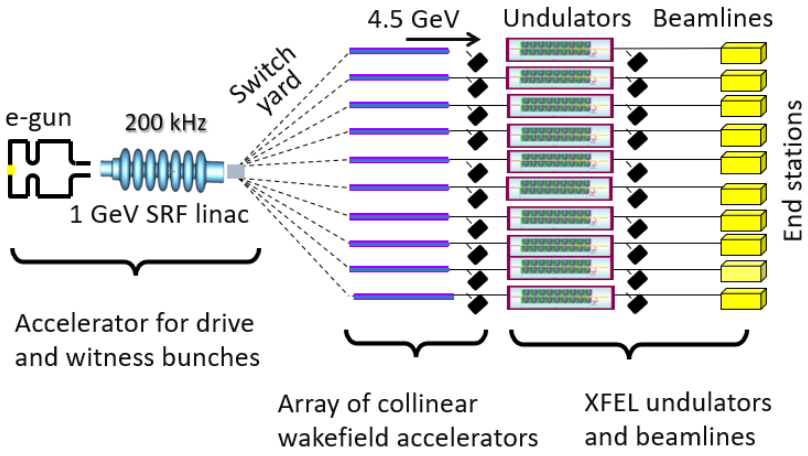

Figure 1. Schematic of the XFEL facility based on the use of the compact collinear wakefield accelerators.

2025 JINST 20 P01023

A drive bunch accelerator (DBA), consisting of a cw superconducting radio frequency (SRF) linac and an SRF electron gun, will sequentially feed all A-STARs with pairs of 10 nC electron drive and 0.1 nC electron witness bunches. The DBA will deliver these pairs to the switch yard in front of the array of A-STARs at a maximum repetition rate of 200 kHz where they will be distributed to different XFELs. A novel force-neutral adjustable phase undulator (FNAPU) [61, 62] will be used in the XFELs to produce coherent X-ray radiation. The facility will be able to cover the spectrum in the tender-to-hard X-ray wavelengths from 1.5 keV to 10.2 keV using an electron beam with energies from 2.0 GeV to 4.5 GeV and a FNAPU undulator with a period of 12.6 mm and a variable undulator parameter K from 1.0 to 1.57, see figure 2. This range of photon energies includes K-edges of 18 atoms from silicon to zinc.

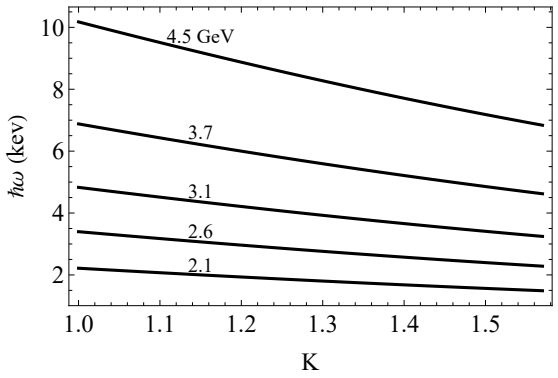

Figure 2. Photon energy $\hbar\omega$ versus undulator parameter K calculated for an undulator with a period of 12.6 mm and different beam energies shown above the lines.

This paper is focused on a description of the A-STAR design. The theory of the wakefield acceleration in the CWA based on a cylindrical corrugated waveguide (CWG) is briefly reviewed in the next section. The design of the main A-STAR components is discussed in section 4. Component testing is discussed in section 5, and the preliminary design of the XFEL is discussed in section 6.

For the reader's convenience concise explanations of the abbreviations and symbols are given at the end of the paper in tables 11 and 12.

3 Review of the theory of the wakefield acceleration

A-STAR is a single-stage accelerator. It uses a single drive bunch and ends when drive bunch electrons decelerate to below 10% of their initial energy. A multi-stage CWA would require more than one drive bunch and precise synchronization between the arrival times of the witness bunch and incoming drive bunches — a challenging task we aimed to avoid. Instead, we opted to maximize accelerator efficiency by utilizing the drive bunch energy in a single stage using the drive bunch with a "doorstep" charge distribution [56, 63], shown in figure 3, to produce a large transformer ratio $\mathcal{R} \equiv \max|E_{\rm acc}|/\max|E_{\rm dec}|$, where $E_{\rm acc}$ is the accelerating field behind the drive bunch, and $E_{\rm dec}$ is the decelerating field inside the drive bunch.

The upper limit for $E_{\rm acc}$ in the CWA depends on $\mathcal{R}$, the loss factor $\kappa_{\|}$ of the CWA, and the total charge of the drive bunch q_0 [64]:

$$E_{\rm acc} \le 2\kappa_{\|}|q_0|\frac{2\mathcal{R}}{1+\mathcal{R}^2}. \tag{3.1}$$

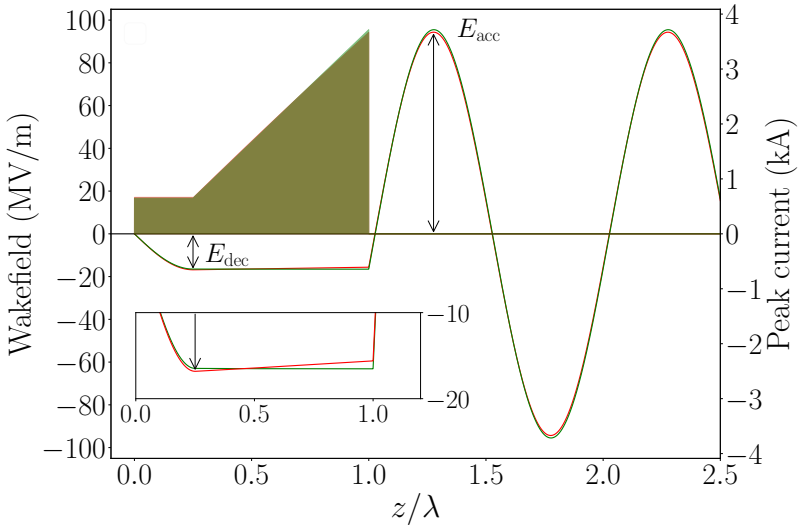

Figure 3. Nominal (green trace) and modified (red trace) "doorstep" distributions and correspondent wakefields calculated using 10 nC bunch charge and loss factor $\kappa_{\|} = 11.8$ kV/pC/m.

It can be reached using a slow wave medium with single-moded Green's function,[1] in which case the transformer ratio approaches a limited value

$$\mathcal{R} \to \sqrt{1 + (kL)^2}, \tag{3.2}$$

where L is the length of the "doorstep" distribution at the base, $k = 2\pi/\lambda$ is the wave vector, and λ is the wavelength of the Green's function.

The pair of eqs. (3.1) and (3.2) conveys a simple physics. The accelerating field behind the drive bunch begins to drop when the electrons begin to occupy a large fraction of the wavelength λ, in which case the cooperative interference of the radiation fields of the individual electrons propagating a slow wave medium begins to weaken and the destructive interference between the radiation fields of the head and tail electrons begins to prevail. This leads to suppression of the decelerating field inside the drive bunch and the accelerating field behind the drive bunch, but with imbalance controlled by the length of the charge distribution in the electron bunch, that can be adjusted to yield a large transformer ratio. As a result, more drive bunch energy could be passed to the witness bunch. This trade-off between the accelerator efficiency and the maximum value of the accelerating field is illustrated in figure 4. In three cases plotted there, the energy gain of a 0.1 nC witness electron bunch was simulated using a drive electron bunch with an initial energy of 1 GeV, a charge of 10 nC, and an initial offset of 5 µm. It is worth mentioning that a deviation from the line begins when the charge distribution starts to elongate as the result of large electron transverse oscillations.

Another important consideration for using the "doorstep" charge distribution for the drive bunch is that it provides the same deceleration of most electrons except for a short section at the beginning of the bunch. It prevents premature termination of the witness bunch acceleration when only a small fraction of the drive bunch electrons reach the lowest energy level and get lost.

[1] It has been shown in [64] that a multi-mode Green's function is less effective in producing a high transformer ratio.

2025 JINST 20 P01023

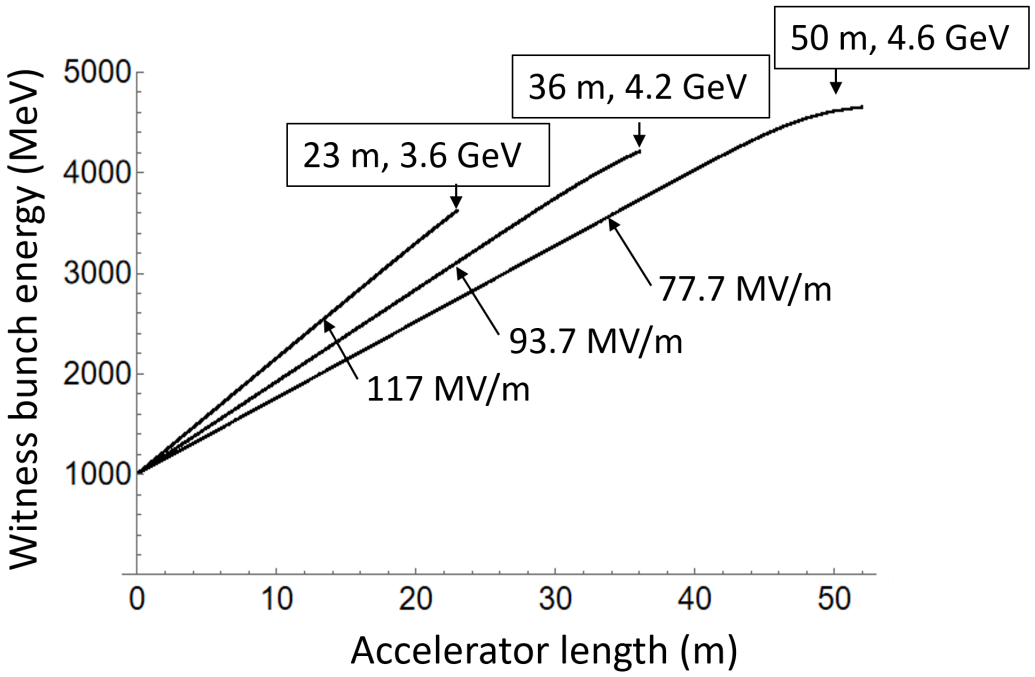

Figure 4. Witness bunch energy gain in the CWA operating with $\mathcal{R} = 3.2$ (left line), 4.2 (center line), and 5.1 (right line). The boxes atop the curves show the accelerator length in meters and the maximum witness bunch energy in GeV at the end of the accelerator. In each case, the accelerator ends before the drive bunch begins losing electrons. The numbers next to the arrows show the accelerating field.

The wakefield produced by the drive electron bunch traveling the CWA can be written [65, 66]

$$E(z) = 2\kappa_{\parallel} \int_0^z G(z - z')q(z')\mathrm{d}z' = 2\kappa_{\parallel} \int_0^z \cos\left[k(z - z')\right]q(z')\mathrm{d}z', \tag{3.3}$$

where G is the Green's function consisting only of a fundamental mode. This is a Volterra integral equation of the first kind for the function $q(z)$ with the trigonometric kernel. If we assume that $E(0) = 0$, then the solution of eq. (3.3) is [67],

$$q(z) = \frac{1}{2\kappa_{\parallel}} \left[E'(z) + k^2 \int_0^z E(x)dx\right], \quad z \le L, \tag{3.4}$$

where $E(z)$ is a known function inside of the drive bunch. Hence, $q(z)$ is defined.

For a given $q(z)$ the upper limit for E_{acc} is solely defined by the loss factor $\kappa_{\parallel}$, which has the maximum value in the case of a single-moded steeply corrugated structure [68–70] and is written below in CGS units

$$\kappa_{\parallel} = \frac{2}{a^2}, \tag{3.5}$$

where a is the minor radius of the CWG. Therefore, a large wakefield can be obtained using the CWG with a small a. However, a kick factor [66] defined for the CWG in CGS units as [70, 71]

$$\kappa_{\perp} = \frac{8}{a^4}, \tag{3.6}$$

2025 JINST 20 P01023

increases too as does the Lorentz force acting in the transverse x and y directions

$$F_\perp(z,s) \propto \frac{\kappa_\perp}{k_1}\int_0^z \sin(k_1(z-z'))q(z')y(z',s)dz'. \tag{3.7}$$

Here k_1 is the wave vector of the CWG's dominant dipole mode, $y(z)$ is the vertical offset of the slice of the drive bunch electrons ($x(z)$ should be used under the integral in the case of the horizontal offset), and s is the distance propagated by the drive bunch in the CWA. $F_\perp$ is responsible for the drive bunch proneness to develop transverse beam-breakup (BBU) instability [72–74]. Since $E \propto 1/a^2$ and $F_\perp \propto 1/a^3$ due to $k_1 \propto 1/a$, this force increases more rapidly than the wakefield as a decreases. A BBU-mitigation technique consists of (i) imparting an energy chirp in the drive bunch [75–77], (ii) embedding the CWG into the row of alternating focusing (F) and defocusing (D) quadrupole magnets (quadrupole wiggler), and (iii) creating the drive bunch with a charge distribution $q(z)$ that supports a dynamic adjustment of the energy chirp concurrently with deceleration of the drive bunch in the CWA caused by the wakefield [78]. The latter is achieved by having a small linear variation in the energy loss inside the drive bunch due to the wakefield such as

$$E'_{\rm dec}(z,s) \propto \frac{1}{\hat{\mathcal{E}}(s)}\frac{d\mathcal{E}}{dz} = \chi \equiv \text{const.}, \tag{3.8}$$

where $\hat{\mathcal{E}}(s)$ is the energy of the reference particle. We solve eq. (3.4) assuming constant $q(z)$ in the range $0 \le z < z_0 = \frac{1}{k}\arccos(\chi/k)$

$$q(z,z_0) = \begin{cases} C, & 0 \le z < z_0\,, \\ C\Big[1 - kz_0\sin(kz_0) + \frac{k^2}{2}z_0^2\cos(kz_0) & \\ \quad + \big(k\sin(kz_0) - k^2 z_0\cos(kz_0)\big)\,z + \frac{k^2}{2}\cos(kz_0)z^2\Big], & z_0 \le z \le L\,, \end{cases} \tag{3.9}$$

$$\text{with } C = \frac{6q_0}{6L + k^2\cos(kz_0)(L-z_0)^3 + 3k\sin(kz_0)(L-z_0)^2}\,.$$

The formula above ensures that both $E(z)$ and $E'(z)$ are continuous within the bunch, see [63]. In the limit $\chi \to 0$, $q(z,z_0)$ describes the "doorstep" distribution proposed in [56].

The red trace in the inset in figure 3 shows the wakefield that is required for the implementation of the dynamic adjustment of the energy chirp illustrated in figure 5. The deviation from a former flat wakefield is small and a minor modification of $q(z)$ that produces it is difficult to notice. It adds a small quadratic component to the linear rise of $q(z)$.

The use of the quadrupole wiggler in the CWA and the energy chirp in the drive bunch aims to gradually increase the betatron oscillation frequency of the drive bunch slices from the head to the tail of the drive bunch following the idea of the Balakin-Novokhatsky-Smirnov (BNS) damping of BBU [75]. Under this condition, the betatron oscillations of none of the bunch slices can be resonantly driven by the transverse wakefields produced by the preceding bunch slices. It has been shown in [78] that the maximum achievable accelerating field solely depends on success in BBU mitigation

$$\max(E_{\rm acc}) \le 1.25\frac{\Delta\mathcal{E}}{\hat{\mathcal{E}}}cB_{\rm q}, \tag{3.10}$$

2025 JINST 20 P01023

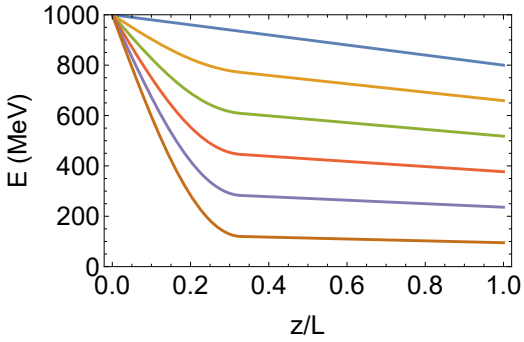

Figure 5. The snapshots of the drive bunch longitudinal phase space taken at equal distances along the accelerator beginning from $s = 0$. Aside from the bunch's first section, the relative magnitude of the energy chirp remains constant with the bunch's deceleration.

where $\Delta\mathcal{E}$ is the head-to-tail energy variation in the drive electron bunch with the head electrons having higher energy, B_q is the magnetic field at the tip of the quadrupole's pole, and c is the speed of light. Using $B_q = 1.6\,\mathrm{T}$ as a practical limit due to soft iron pole magnetization saturation and $\Delta\mathcal{E}/\hat{\mathcal{E}} = 15\%$ as a practical limit for the energy chirp that can be obtained in the DBA, we calculate $\max(E_{acc}) \leq 90\,\mathrm{MV/m}$.

As the drive bunch propagates the CWA, the electrons produce the wakefield and lose energy. Therefore, the strength of focusing by the quadrupoles must decrease concurrently with the change in the beam energy. Otherwise, the frequencies of betatron oscillations of electrons will increase and reach the parametric resonance causing the inevitable loss of electrons. Adaptive focusing suggested in [78] is accomplished by reduction of the quadrupole's length L_q, i.e.,

$$L_q(s) = L_{q(s=0)}\sqrt{1 - \varkappa s}, \tag{3.11}$$

where $\varkappa = |eE_{dec}|/\hat{\mathcal{E}}_{(s=0)}$, and e is the electron charge. It produces a gradual increase of the phase advance of the betatron oscillations per unit length of the accelerator that results in faster decoherence of betatron oscillations along the bunch.

The implementation of the concepts of the dynamic energy chirp and adaptive focusing are necessary prerequisites for obtaining the maximum accelerating field defined in (3.10).

In summary, the maximum accelerating field in the CWA is constrained by the onset of the BBU to $\sim 90\,\mathrm{MV/m}$. Consequently, the goal for the A-STAR design is to obtain this field considering practical constraints. An inspection of (3.1) shows that only q_0, $\mathcal{R}$, and a can influence E_{acc}. However, practical considerations limit q_0 to less than 10 nC due to a large beam power in the DBA at the anticipated megahertz-scale bunch repetition rate. Obtaining a substantial energy gain for the witness bunch in the single-staged CWA requires $\mathcal{R} \gtrsim 5$. The CWG's manufacturing challenges impose the requirement $a \geq 1\,\mathrm{mm}$. Thus, using $a = 1\,\mathrm{mm}$, $q_0 = 10\,\mathrm{nC}$, and $\mathcal{R} = 5$ in (3.1), we calculated $E_{acc} \approx 90\,\mathrm{MV/m}$. According to (3.10), the energy chirp $\Delta\mathcal{E}/\hat{\mathcal{E}} \geq 15\%$ must be used to keep the drive bunch stable.

4 A-STAR component design and fabrication

The A-STAR CWA is composed of many 0.5 m-long accelerating modules placed in series, each containing the corrugated waveguide (CWG) supported by a strongback and surrounded by the quadrupole wiggler, and a short transition section containing electromagnetic couplers, diagnostics, vacuum pumping ports, water cooling outlets, and bellows (see figure 6).

2025 JINST 20 P01023

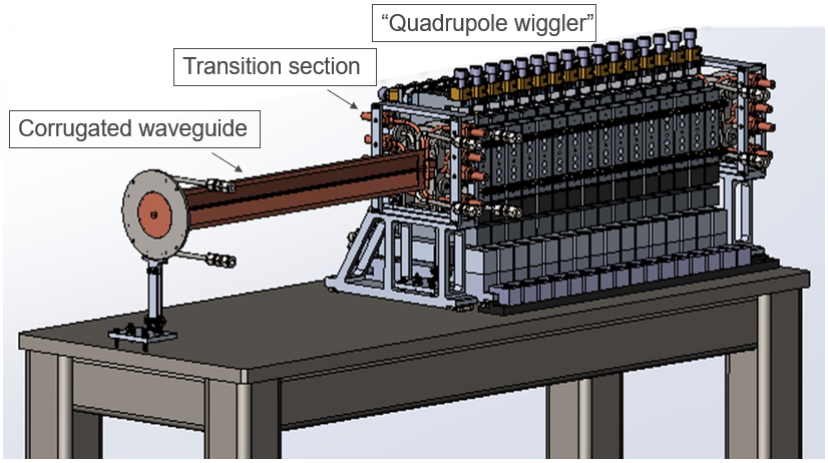

Figure 6. Two 0.5 m-long modules of the CWA, showing the module on the left with the quadrupole wiggler removed.

4.1 Design and fabrication of the corrugated waveguide

The CWG is a round metallic pipe with grooves around the inner circumference of the wall, as shown in figure 7. The minor radius a of the CWG is the distance between the center axis of the waveguide and the tips of the corrugation teeth. Here, we refer to the raised part of the profile as the corrugation tooth and the space between adjacent teeth as the vacuum gap. We assign symbols t and g to define the tooth and gap widths. We use d to define the groove depth. The radii of the tooth tip r_t and vacuum gap floor r_g are connected by a flat surface called the sidewall, and the overall dimensions of the corrugation are small compared to the minor radius a.

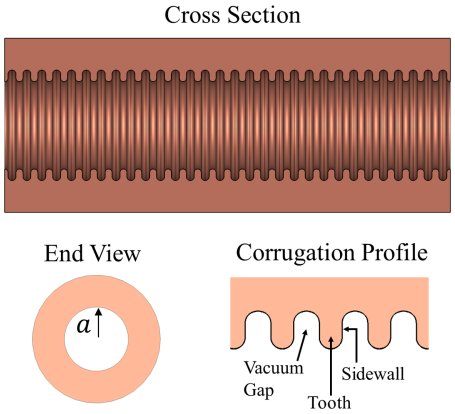

Figure 7. Cylindrical corrugated waveguide (CWG) with minor radius a.

4.1.1 Electromagnetic design of the corrugated waveguide

The electromagnetic CWG design process consisted of finding corrugation geometries to minimize peak surface fields and to maximize the loss factor and group velocity of the TM_{01} mode of Čerenkov radiation — a fundamental axial mode of the CWG structure. It was also required that the corrugated structure was predominantly single-moded, which is the preferred operating condition for obtaining the

2025 JINST 20 P01023

highest accelerating field [64]. In pursuit of these goals, the CWG was modeled as a periodic structure of infinite length by employing a periodic boundary condition derived from beam-wave synchronicity

$$\phi = \frac{360 f_m p}{c}. \tag{4.1}$$

Here ϕ is the phase advance per cell in degrees, f_m is the frequency of the TM_{01} mode, c is the speed of light, and $p = t + g$ is the corrugation period.

Electromagnetic simulation of the TM_{01} accelerating mode was performed using the eigenmode solver in CST Microwave Studio [79]. The corrugated structures were simulated at three fixed frequencie — 160 GHz, 180 GHz and 200 GHz — to characterize its frequency-dependent behavior. These frequencies were parametrized by their respective dimensionless aperture ratios defined as $\hat{a} = a/\lambda$, where λ is the wavelength of the TM_{01} synchronous mode. Additional normalization ratios d/a, p/a, and $\xi = \frac{g-t}{p}$ were used to generalize the study to corrugated structures of any size and frequency [80]. Parametric analysis began by treating the corrugation depth d as a dependent variable determined by the aperture ratio, eliminating it from the parameter sweeps. This was done by using an iterative optimization process to find the corrugation depths required to achieve the predetermined frequencies. The resulting corrugation depths normalized by a are plotted in figure 8. In all cases, the corrugation depth decreases with increasing aperture ratio, where shallower corrugations produce higher synchronous TM_{01} frequencies.

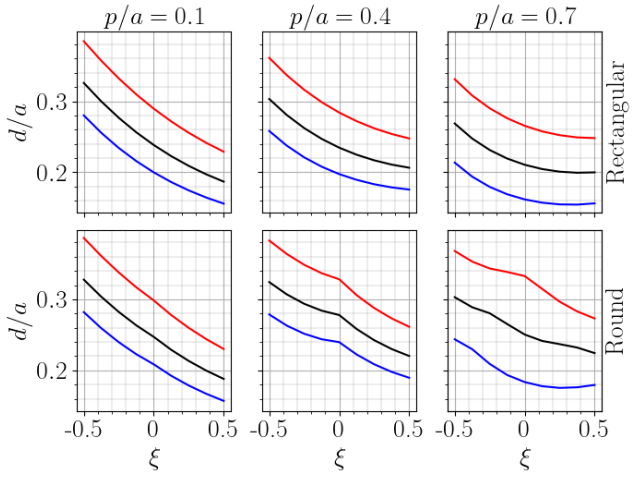

Figure 8. Corrugation depths d calculated for aperture ratios of $\hat{a} = 0.53$ (red), 0.60 (black), and 0.67 (blue) for the rectangular corrugations (top) and corrugations with maximum corner radii $r_t = r_g = \min(t, g, d)/2$ (bottom).

Each synchronous eigenmode solution of the periodic structure is characterized by a wakefield loss factor $\kappa_\parallel$, group velocity v_g, and wakefield attenuation constant α. These parameters determine how the electron beam interacts with the given mode and the propagation characteristics of the corresponding wakefield. Figure 9 shows how these parameters depend on the geometry [80] for a CWG with minor radius $a = 1$ mm and electrical conductivity $\sigma = 4 \times 10^7\ \mathrm{S\,m^{-1}}$, which is lower than the oxygen-free copper conductivity. The scaling $\kappa_\parallel \propto a^{-1/2}$ and $\alpha \propto a^{-3/2}\sigma^{-1/2}$ can be used to project the results for various a and σ. Structures with shorter corrugation periods produce larger group velocities and wake potentials making it desirable to choose the period as short as possible.

2025 JINST 20 P01023

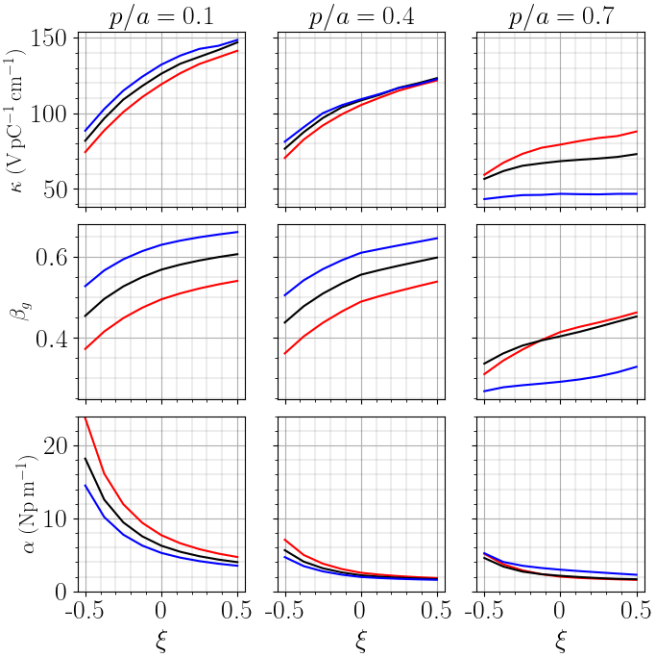

Figure 9. Loss factor $\kappa_\parallel$, relative group velocity $\beta_g = v_g/c$, and attenuation constant α for the maximum radii geometry with $\hat{a} = 0.53$ (red), 0.60 (black), and 0.67 (blue). Plotted for a CWG with minor radius $a = 1$ mm and electrical conductivity $\sigma = 4 \times 10^7$ S m^{-1}.

As the period shrinks, $\kappa_\parallel$ approaches a maximum value defined by eq. (3.5) for a single-moded steeply corrugated structure with $d \gtrsim p$ [69].

The maximum attainable accelerating gradient in the CWA is limited by several factors, including pulse heating and RF breakdown due to the peak surface fields and modified Poynting vector exceeding certain threshold values [57, 81, 82]. The simulation results in figure 10 show that the peak electric and magnetic fields always increase with increasing aperture ratio, meaning higher choices of frequency

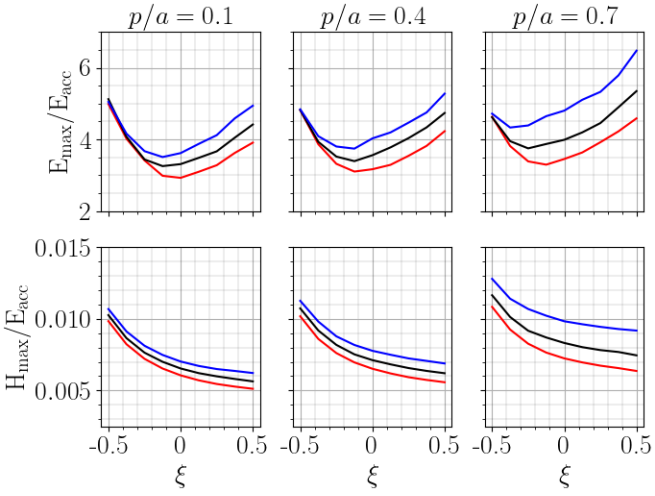

Figure 10. Normalized peak surface E_{max} (V m^{-1}) and H_{max} (A m^{-1}) fields for the maximum radii corrugation geometry with $\hat{a} = 0.53$ (red), 0.60 (black), and 0.67 (blue).

2025 JINST 20 P01023

for the TM_{01} synchronous mode result in higher peak fields for a given accelerating gradient. This observation is consistent with the results reported in [83]. Further refinement of the geometry requires experimental determination of where RF breakdown is most likely to occur in order to reduce the peak fields in those regions.

Thermal loading of the corrugated waveguide places a limit on the maximum repetition rate of the electron bunches in the accelerator f_r. The thermal loading depends on the electromagnetic properties of the TM_{01} mode, the length of the corrugated waveguide, and the conductivity of the wall material. Achieving a high repetition rate requires active cooling of the structure and an optimally designed corrugation profile. Here we focus on designing a corrugation that minimizes the steady state thermal loading and transient pulse heating. The thermally induced stresses due to temperature gradients in the wall pose additional design considerations that are discussed further in [84] and section 4.1.2.

Since $\beta_g < 1$, the length of the RF pulse behind the bunch grows as it traverses the structure. This causes the thermal energy density deposited in the CWG wall to increase along the direction of propagation. At a distance s from the beginning of the CWG, the field strength of the RF pulse induced by the electron bunch entering at time $t = 0$ is [80]

$$P^{1/2}(s,t) = \sqrt{\frac{E_{\mathrm{acc}}^2 v_g}{2\kappa_{\parallel}(1-\beta_g)}} e^{\frac{-\alpha(v_g t-\beta_g s)}{1-\beta_g}} \cos\left(k\left(ct-s\right)\right) \Pi\left(\frac{2v_g t - s(1+\beta_g)}{1-\beta_g}\right). \tag{4.2}$$

Here the field strength is defined in units of $\sqrt{\mathrm{W}}$ for consistency with the units provided by the CST Microwave Studio simulation, and $\Pi(x)$ is the rectangular window function

$$\Pi(x) = \begin{cases} 1 & |x| < 1/2 \\ 0 & \text{else.} \end{cases} \tag{4.3}$$

The derivative of the one-dimensional energy dissipation distribution $Q_{\mathrm{diss}}(s)$ along the corrugated structure is obtained by multiplying P from eq. (4.2) by the attenuation constant α and integrating the product over time from $t = 0$ to $t = \infty$:

$$\frac{dQ_{\mathrm{diss}}(s)}{ds} = \frac{E_{\mathrm{acc}}^2}{4\kappa_{\parallel}}\left(1 - e^{-2\alpha s}\right). \tag{4.4}$$

Using (4.4) as a starting point, we calculated in [80] the wakefield power dissipation in the 0.5 m-long accelerator module $P_{\mathrm{diss}} = Q_{\mathrm{diss}} f_r$, the upper bound for power density impinging the CWG wall, and the transient temperature rise. These parameters are given in table 1 together with other CWG parameters discussed in this section and finalized during computer optimization of the corrugation profile.

Finally, we chose the frequency for the CWG's fundamental accelerating mode TM_{01} to be 180 GHz and the frequency for the CWG's dipole mode HEM_{11} to be 10 GHz higher. These are the highest frequencies compatible with the design and fabrication challenges of the electromagnetic couplers discussed in section 4.2.4. Table 2 shows parameters related to these two main electromagnetic modes of the CWG.

4.1.2 Impact of the beam-induced heating of the corrugated waveguide

The electromagnetic wave of Čerenkov radiation propagates downstream of the CWG with a slower group velocity than the beam velocity. Interacting with corrugations, it excites surface currents

2025 JINST 20 P01023

Table 1. A-STAR key operating parameters.

Parameter		
a	1 mm	corrugation minor radius
d	264 µm	corrugation depth
g	180 µm	corrugation vacuum gap
t	160 µm	corrugation tooth width
$r_{t,g}$	80 µm	corrugation corner radius
p	340 µm	corrugation period
ξ	0.06	spacing parameter
$\mathcal{R}$	5	transformer ratio
q_0	10 nC	bunch charge
E_{acc}	90 MV m^{-1}	accelerating gradient
E_{max}	325 MV m^{-1}	peak surface E field
H_{max}	610 kA m^{-1}	peak surface H field
ϕ	74°	phase advance
f_r	20 kHz	repetition rate
P_{diss}	1050 W	power dissipation per module
L_{acc}	50 cm	accelerator module length
W	55 W/cm^2	power density upper bound
ΔT	9.5°K	pulse heating

Table 2. A-STAR synchronous electromagnetic mode characteristics. The loss factor $\kappa_{\parallel}$ for the HEM_{11} mode scales with the square of the beam offset and is given for the offset of 1 µm. The attenuation coefficient α is given for a structure with conductivity of 4×10^7 S m^{-1}.

	TM_{01}	HEM_{11}	Units
f	180	190	GHz
$\kappa_{\parallel}$	1.18×10^{16}	2.19×10^{10}	V C^{-1} m^{-1}
β_g	0.57	0.62	None
α	2.31	1.96	Np m^{-1}

responsible for the CWG heating. As shown in figure 6, the CWG is embedded into a "bow-tie"-shaped copper structure called the chamber for brevity. The drive beam, consisting of 10 nC bunches propagating at a 10 kHz bunch repetition rate, deposits on the chamber the steady state power that gradually increases along the 0.5 m length of the CWG from 0.03 W/cm at the beginning to 39.75 W/cm at the end. The chamber has two 6 mm-diameter channels, one above and one below the corrugations. They are used to propagate the deionized water with a velocity of 3 m/s. The water flows in the direction opposite to the beam motion. The size of these channels and the choice for their location are severely constrained by the quadrupoles surrounding the structure. The "bow-tie" shape for the chamber constrains heat transfer from the hottest locations on corrugations to water.

The electromagnetic field calculation performed with CST Microwave Studio [79] defined the heat load, and COMSOL Multiphysics [85] was used to model chamber cooling [84]. The copper properties that were used in the calculation are listed in table 3. Note that the value of electrical

2025 JINST 20 P01023

Table 3. Material Specifications.

Parameter	Value	Units
Thermal conductivity	400	$\mathrm{W/(m\,K)}$
Electrical conductivity	2.3×10^7	$\mathrm{S/m}$
Linear expansion coefficient	17×10^{-6}	$\mathrm{1/K}$
Specific heat	385	$\mathrm{J/(kg\,K)}$
Modulus of elasticity	190	GPa
Poisson's ratio	0.35	

conductivity was intentionally degraded by a factor of 2.5 to perform conservative calculations for the electroformed copper whose actual surface roughness and electrical conductivity were not known.

Figure 11 shows the steady state temperature distribution in the chamber and corrugations. The heating produces a temperature gradient that leads to progressively higher thermal expansion in the downstream direction. The stress from the differential expansion can cause cracking, arcing, and beam loss if it exceeds the material tensile yield threshold. The analysis of von Mises stress was performed, and figure 12 shows the area of corrugations where stress is highest. As expected, the stress varies along the corrugation profile reaching maximum values where the surface magnetic field is the highest.

We note that the areas of high stress are localized within the electroformed copper. Studies have shown [86, 87] that the yield stress of electroformed copper with a grain size of ~ 1 µm can reach values between 200 MPa to over 400 MPa. This high yield strength is attributed to the Hall-Petch effect [88, 89], which predicts an increase in yield strength in polycrystalline materials like metals as the grain size decreases. Since the CWG stress scales linearly with f_r, these findings indicate that by optimizing the electroforming process to control grain size, the $f_r \simeq 50$ kHz can be achieved. However, low-temperature brazing must be used in fabrication of the CWG because high temperature leads to grain growth and decreases the material's strength.

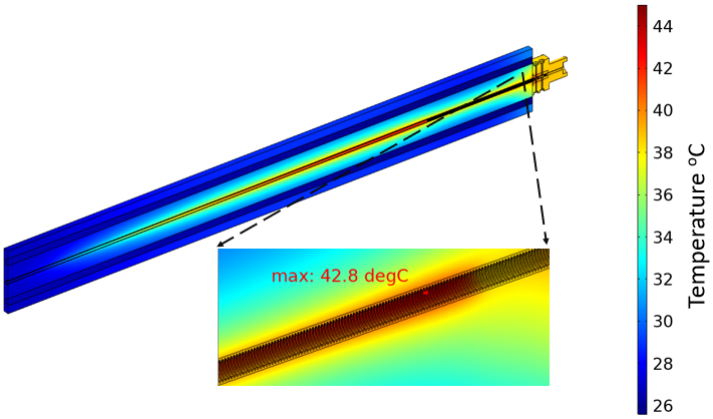

Figure 11. Steady state temperature distribution in the chamber calculated using a 10 kHz bunch repetition rate. The electron bunch enters the structure from the left side. The maximum temperature of 42.8°C is near the end of the CWG where the electromagnetic pulse is the longest, as shown in the inset. The water inlet temperature is 25.6°C. The inset shows the region with the highest temperature.

2025 JINST 20 P01023

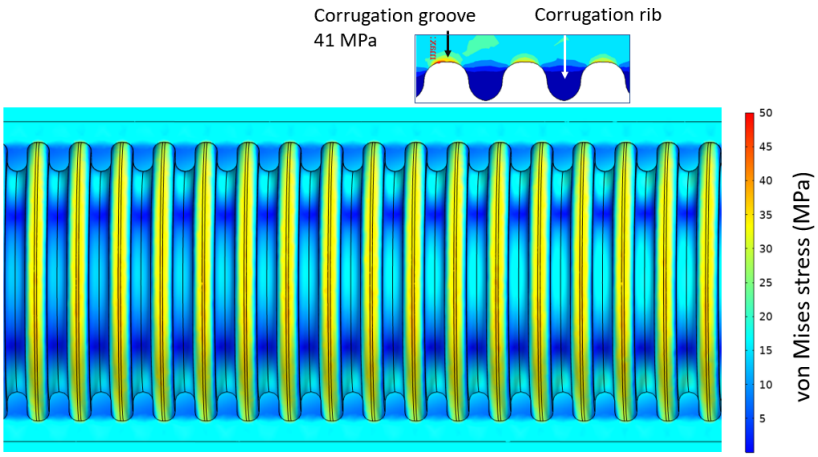

Figure 12. Von Mises stress. This section of the CWG, located 40 mm upstream of the transitions section, has the highest stress of 41 MPa.

4.1.3 Fabrication of the corrugated waveguide

Electroforming (see [90] and references therein) is the most suitable method for making small-sized CWGs [91]. An aluminum (Al) mandrel is produced by micro-machining. After precision masking is applied, the mandrel is placed in a plating tank for several days where copper sulfate with proprietary additives is used for copper deposition. Afterwards, the mandrel is placed in a hot bath of NaOH to chemically dissolve the aluminum. The complete etching of aluminum leaves behind the plated structure as the final product. The corrugation dimensions reflect the manufacturing quality of the aluminum mandrel geometry. The surface roughness (Ra) of the electroformed components depends on the deposition thickness and the surface roughness of the Al mandrel. The CWG fabrication requires a 0.5 mm Cu deposition thickness. With this thickness, it is possible to obtain Ra $\simeq$ 700 nm using a hybrid electrochemical process [92], in which case the surface roughness of the Al mandrel will likely determine the surface roughness of the final product.

The maximum CWG length is limited by the ability to maintain straightness of the 2.53 mm-diameter Al mandrel during machining. Since making a 0.5 m-long waveguide in one piece is not feasible, we braze five 98 mm-long sections using a brazing alloy containing 88% Au and 12% Ge that is suitable for brazing with a maximum temperature of 365°C, as shown in figure 13.

Metrological analysis of the CWG section mandrel shown in figure 14 indicates an excellent uniformity in the corrugation pattern and a good surface finish. The tooth's height and width are 252.7 $\pm$ 1.5 µm and 175.9 $\pm$ 2.0 µm, correspondingly. The design values are 264 µm and 160 µm. We estimate that these errors can lead to up to a 4% shift in the frequency of the fundamental mode of the wakefield.

The Al mandrels develop a sag during machining with the measured offsets in the center distributed anywhere from 40 to 100 µm with a mean value of 65 µm and a standard deviation of 18 µm. These offsets have been reduced to below the acceptable tolerance of 4 µm with a manual straightening using a fixture that is controlled by observation on an optical comparator with a modest resolution of approximately 2.5 µm.

Once electroforming of the mandrel is complete, the plated electroform is machined while still on the mandrel with reference to the masked surfaces. EDM is performed using a custom-made

2025 JINST 20 P01023

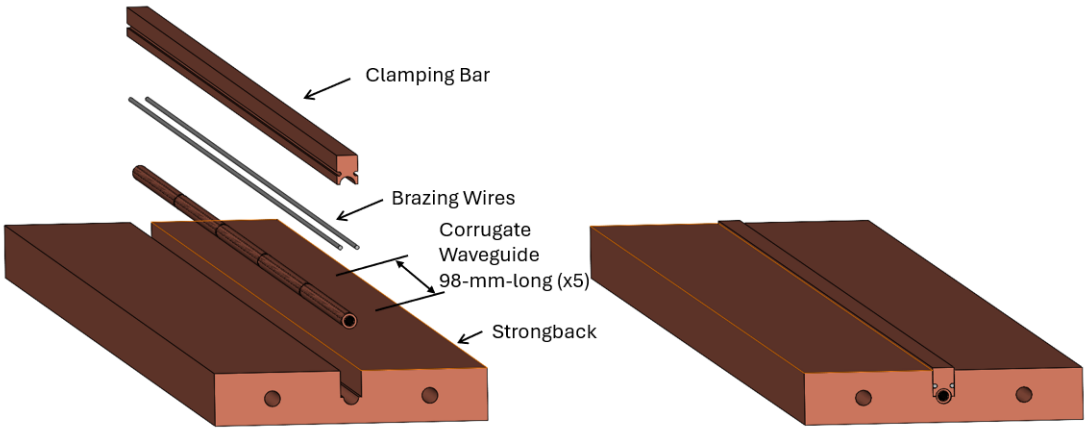

Figure 13. Brazing the 0.5 m-long waveguide assembly.

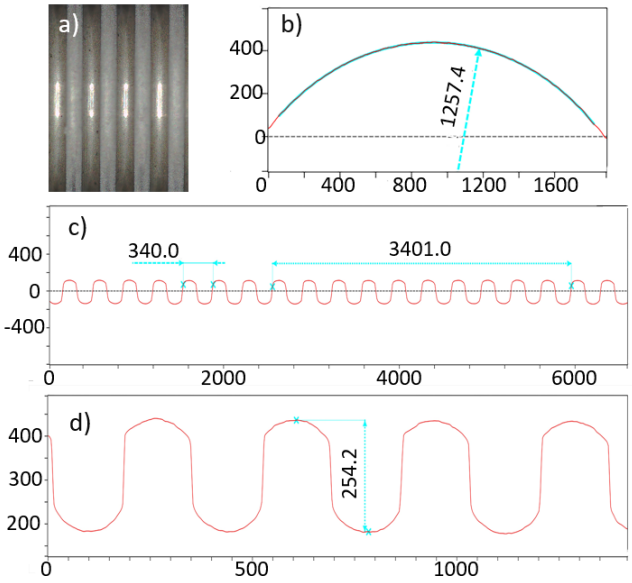

Figure 14. (a) Fragment of the mandrel viewed under the microscope with 150 times magnification. (b) Radius profile of the mandrel 'tooth' that will form the CW 'groove'. (c) Corrugation profile measured along a short section of the CWG indicating uniform periodicity. (d) Corrugation detail indicating groove depth. All dimensions are in microns.

tungsten electrode to obtain the 2.9 mm outside diameter (OD) of the plated mandrels required by the design. An extra Cu layer was deposited during electroforming to accommodate possible plating depth irregularities and to obtain a concentric OD with respect to the corrugation profile. The high precision was achieved by taking the ends of the Al mandrels (masked during electroforming) as reference points for finding the CWG axis (see figure 15). Straightening of the plated mandrels was performed after completion of the EDM OD machining.

Before the final step of dissolving the aluminum, high-precision cuts were made at the ends of the trimmed mandrels in the middle of the last corrugation tooth on both ends of the waveguide using the reference grooves machined at both ends of the Al mandrels (see figure 15).

2025 JINST 20 P01023

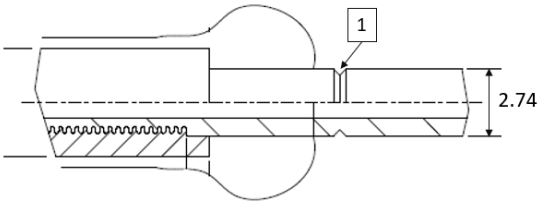

Figure 15. Drawing of the end of the plated mandrel showing the diameter of the masked aluminum in millimeters and the location of the reference groove (1).

Dimensional analysis was performed on two CWG samples that were cut in half longitudinally by wire EDM to expose the internal corrugations, see figure 16(a). The longitudinal profile measurements shown in figure 16(b) indicate excellent uniformity with the height of the corrugations, as well as with the periodicity. The average height of the corrugations is 249.7 µm, periodicity is 340.7 µm, and deviations are within ± 5 µm. No cumulative error is evident across 10 periods. The cross-sectional profile in figure 16(c) indicates a uniform thickness of the deposited Cu. The small "bumps" evident in the center of the profile are optical artifacts resulting from the high reflectivity of the Cu surface. Figure 17 shows measurements of the internal corrugation radii for both the teeth and the grooves.

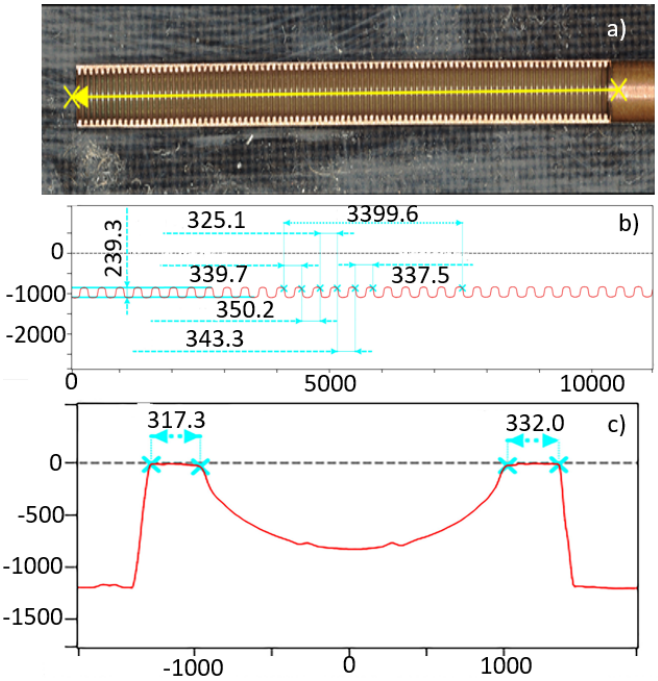

Figure 16. (a) A fragment of the CWG with one half open. (b) Longitudinal profile of the corrugations measured along the line at the bottom of the CWG. (c) Cross-sectional profile measured in the middle of the tooth. All dimensions are in microns.

Surface roughness is difficult to quantify due to the compound curvature features, since the height differences are distorted by the curvature. However, a profile graph of diagonally cut images in figure 18(c) qualitatively shows the regularity of the corrugated geometry. The images in figure 18(a), 18(b) indicate a good surface roughness, although we plan further improvement

2025 JINST 20 P01023

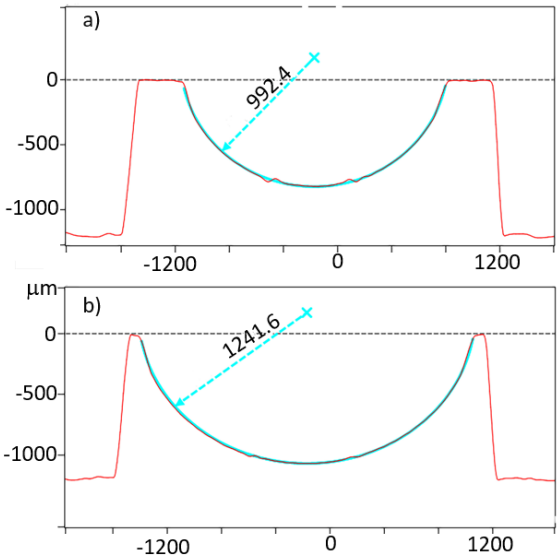

Figure 17. The corrugation radii for (a) groove and (b) tooth. All dimensions are in microns.

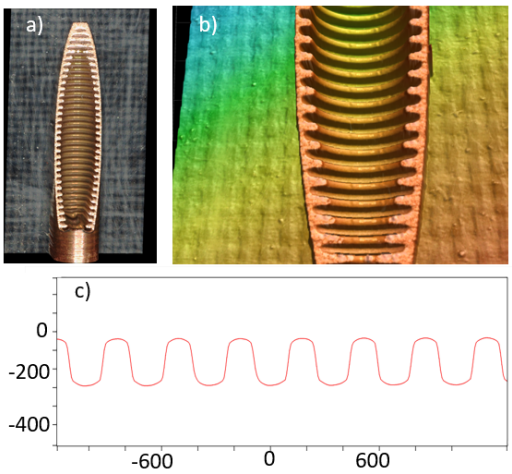

Figure 18. Photographic images of (a) a diagonally cut CWG segment at 100 times magnification, (b) a 3D rendering of the diagonally cut segment, and (c) a profile graph of the corrugation. All dimensions are in microns.

using the hybrid electrochemical process. Small "bumps" seen next to the center are optical artifacts rather than actual surface distortions.

4.1.4 Vacuum analysis and measurements

For vacuum calculations [93], we modeled the CWG as a smooth tube with an effective diameter of 2.26 mm and an effective length of 0.95 m that has the same surface area as a 2 mm-diameter, 0.517 m-long CWG. Assuming the use of pumps on both sides of the tube and using an outgassing coefficient of 3.6×10^{-11} Torr L s^{-1} cm^{-2} [94, 95], we calculated, using COMSOL, the vacuum pressure limited by the tube's conductance as a function of the distance along the tube length, see figure 19. Performing another set of calculations we found that the beam emittance growth in the

2025 JINST 20 P01023

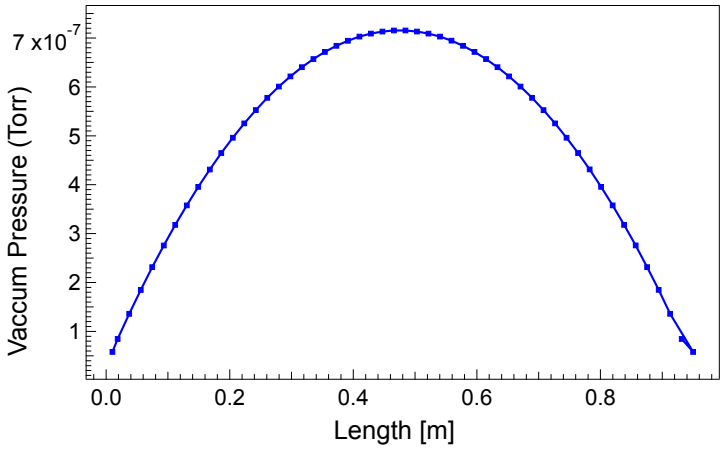

Figure 19. Molecular flow simulation result of the total pressure for an equivalent 0.95 m-long copper tube.

accelerator due to multiple Coulomb scattering of electrons [96] is negligible at the average vacuum level of 4×10^{-7} Torr, consisting only of 10^{-7} mm · mrad. This result suggests that a much poorer vacuum can be used if permitted by consideration of the electrical breakdown.

We fabricated a 152 mm-long mock-up vacuum chamber containing three 2.1 mm-inner-diameter, 50 mm-long oxygen-free copper tubes without corrugation. The machined chamber has a thin section in the middle required for the real CWG, as seen in figure 20. It was pumped down for 48 hours, achieving 4.5×10^{-7} Torr before baking started. Figure 21 shows the vacuum during baking. After the temperature ramp-down, the vacuum pressure was 1×10^{-7} Torr. The final pressure, 8.5×10^{-8} Torr, was measured 24 hours later. The vacuum gauge was placed at the opposite end of the pumping port so that the structure was in the middle. To obtain this vacuum pressure in the calculation, we had to use 7×10^{-7} Torr L s^{-1} cm^{-2} for the outgassing coefficient, which is not surprising considering the typical uncertainty reported in the literature [94, 95].

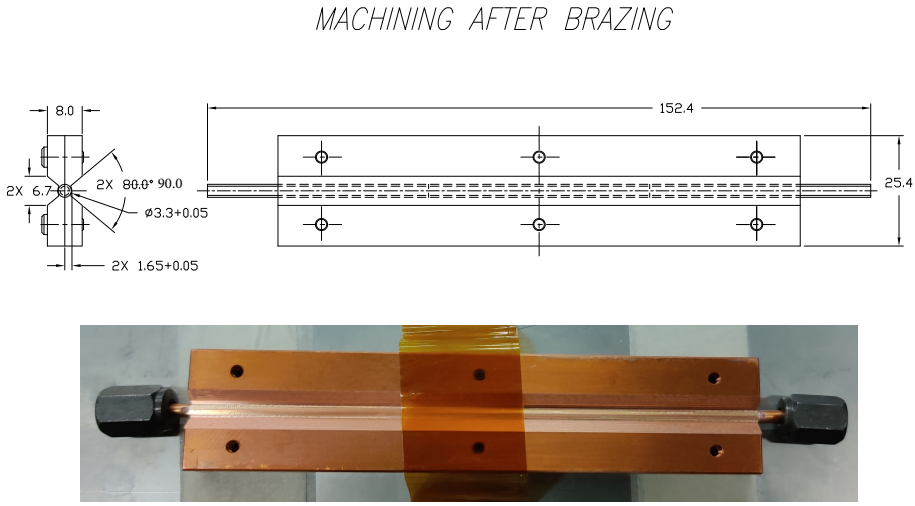

Figure 20. Test piece of the vacuum chamber showing dimensions (top) and the machined chamber (bottom).

2025 JINST 20 P01023

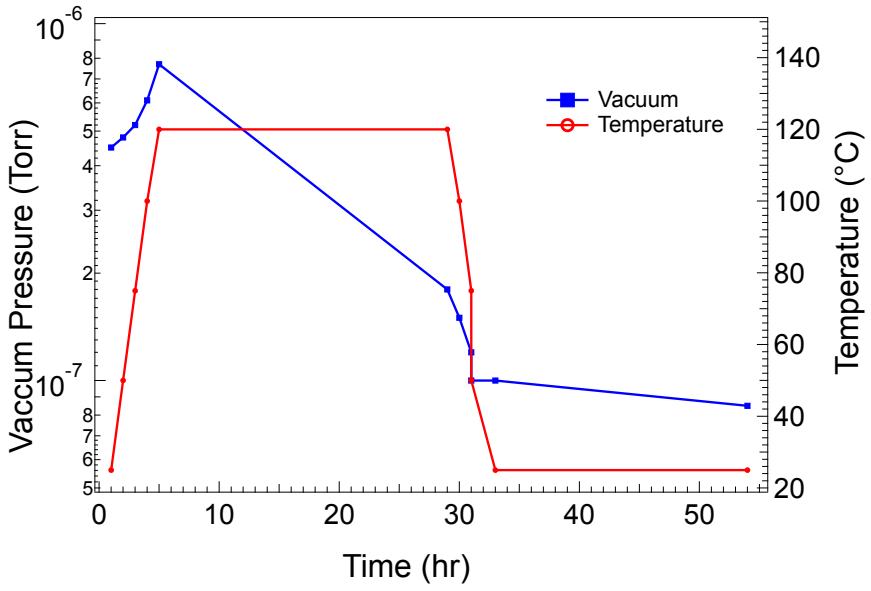

Figure 21. Chamber vacuum testing before, during, and after the baking. The blue line shows the vacuum, the red line shows the baking temperature.

4.2 Design and fabrication of the transition section between accelerator modules

The transition section (TS) contains vacuum pumping ports, bellows, and electromagnetic couplers [97]. The electromagnetic design of the TS is focused on two couplers designated for extracting the 180 GHz TM_{01} accelerating and 190 GHz HEM_{11} dipole electromagnetic modes. Since not all the energy deposited by the drive bunch in the CWG is absorbed by the witness bunch and dissipated in the CWG walls, the TM_{01} coupler is used to extract the residual energy from the accelerator to reduce the thermal load on subsequent CWG structures. The HEM_{11} mode is present in the CWG when electrons in the drive bunch propagate off-axis. Since the HEM_{11} mode in the CWG converts primarily to a TE_{11} mode as it propagates to the cylindrical waveguide input of the TS, we include a TE_{11} coupler, referred to as the integrated offset monitor (IOM), to measure the power in the HEM_{11} mode originating from the upstream accelerator section. Integrating the RF power output from the IOM with a bolometer provides an effective measure of the drive bunch's stability as demonstrated in section 4.2.2.

4.2.1 Coupler's design

Couplers with wide bandwidth are desired to accommodate manufacturing tolerances of the CWG, which shifts the synchronous TM_{01} center frequency by roughly 1 GHz per 1 µm of error in corrugation depth. The second design goal was to minimize the peak surface fields to levels below those in the CWG. As illustrated in figure 22, the TM_{01} coupler consists of a four-way rectangular waveguide cross, connected to a cylindrical waveguide via tapers and a circular cavity. Immediately following the waveguide cross is an RF choke, which reflects the TM_{01} mode. When the incident TM_{01} wave encounters the coupler cross, a portion is transmitted to the choke where it is reflected back through the coupler cross with a phase shift. The length of the spacer between the choke and the coupler cross is chosen such that the phase-shifted wave perfectly cancels the initially reflected wave incident on the coupler cross for the design frequency of 180 GHz.

2025 JINST 20 P01023

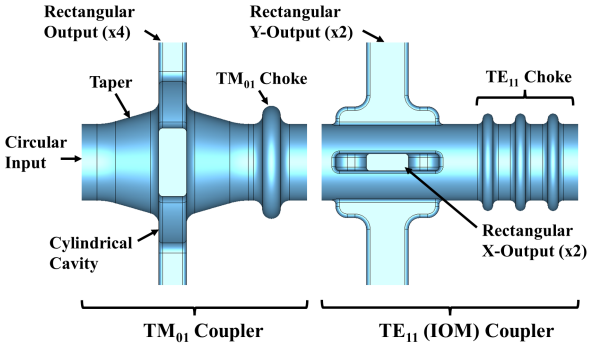

Figure 22. Vacuum space of the TM_{01} and TE_{11} couplers in the transition section.

The RF characteristics of the optimized TM_{01} coupler are illustrated in figure 23. The TM_{01} mode coupling efficiency at 180 GHz is 99.1% with 3 dB bandwidth of 25 GHz [97]. Since the TM_{01} coupler must remain transparent to the TE_{11} mode, TE_{11} transmission through the coupler cross was used as a secondary objective function to be maximized around the 190 GHz center frequency of the IOM.

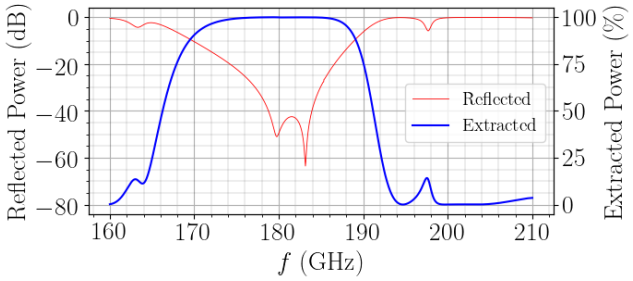

Figure 23. Reflection and extraction of the TM_{01} mode from the TM_{01} coupler. The extracted power is divided equally among the four rectangular waveguide outputs.

The single bunch impulse power at the end of the 0.5 m-long CWG due to the TM_{01} mode is shown in figure 24. The average power going to the TM_{01} mode coupler produced by the train of such pulses proceeding at a 20 kHz repetition rate is 670 W.

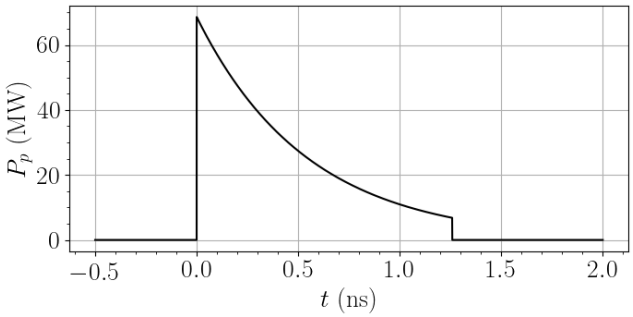

Figure 24. Power envelope of the TM_{01} mode incident to the TS calculated for a "doorstep" charge distribution with $L = 1.3$ mm using a 10 nC bunch charge and reduced copper conductivity of $\sigma = 4 \times 10^7$ S m^{-1}.

Design of the TE_{11} coupler for the IOM followed a similar approach to the TM_{01} coupler, with the simplification that only a single objective function was needed in the optimization. The design

2025 JINST 20 P01023

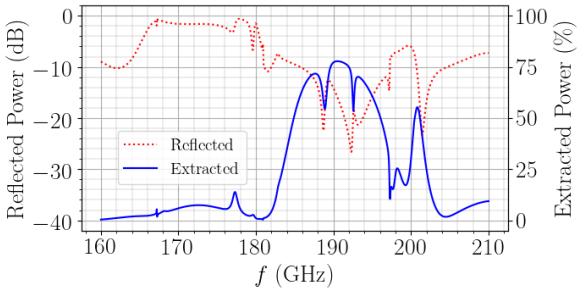

Figure 25. TE_{11} extraction and reflection from the transition section including the TM_{01} coupler before the IOM.

has two pairs of orthogonal rectangular waveguide outputs corresponding to the two polarizations of the TE_{11} mode, as shown in figure 22. The broadwalls of the rectangular waveguide outputs were stepped to a wider dimension at the interface to the circular waveguide to improve coupling efficiency, and the short walls were kept narrow to reduce local wakefield power induced by the drive bunch passing through the structure. The extracted power is 75% at 190 GHz with a 3 dB bandwidth of approximately 16 GHz, see figure 25.

The peak electromagnetic surface fields, transient pulse heating, and steady state thermal power dissipation all pose limitations on the operation of the transition section. As a design goal, the peak surface fields inside the transition section were required to remain below those in table 1 for the CWG. The peak surface fields produced by the TM_{01} RF pulse are shown in figure 26. The maximum E and H fields occur at the interface of the rectangular waveguide to the tapered cylindrical waveguide.

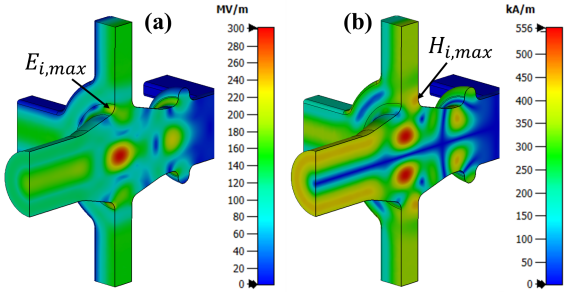

Figure 26. Maximum E-field (a) and H-field (b) for the incident TM_{01} mode from the CWG with 68 MW peak pulse power. Showing $E_{i,\max} = 210\,\mathrm{MV\,m^{-1}}$ and $H_{i,\max} = 448\,\mathrm{kA\,m^{-1}}$.

4.2.2 Integrated offset monitor

The HEM_{11} mode of the CWG excited by the off-axis particles is used for measuring the approximate radial offset of particles in the drive bunch. When the HEM_{11} mode passes from the CWG into the smooth cylindrical waveguide at the input of the transition section, roughly 90% of the power converts to the TE_{11} mode and 10% to the TM_{11} mode of the circular waveguide. Extracting the TE_{11} mode with the TE_{11} coupler, referred to as the integrated offset monitor (IOM), and integrating the RF power with a bolometer yields a measurement of the total HEM_{11} mode energy excited by the bunch. This energy scales approximately with the integrated radial offset of the particles in the bunch and is indicative of the overall stability of the bunch within the CWG module [97].

2025 JINST 20 P01023

An example drive bunch trajectory through the CWA is shown in figure 27. The initial offset of the bunch causes oscillation of the center of charge as the bunch propagates through the continuous channel of focusing and defocusing quadrupoles surrounding the CWG. The bunch is injected with an energy chirp that leads to BNS damping and eventual stabilization [75, 78], as shown in figure 27.

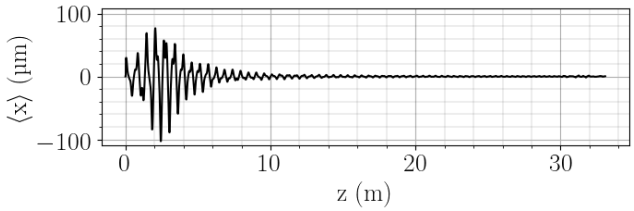

Figure 27. Radial offset of the drive bunch center of charge propagating through the CWA. The trajectory is calculated for a 10 nC drive bunch with a 15% energy chirp and an initial offset of 30 μm from the center axis.

A closeup view of the center of charge trajectory between 2 m and 2.5 m, corresponding to the fifth accelerator module, is shown in the top panel of figure 28. Snapshots of the bunch curvature at three locations in the module are shown in the middle panel, where the tail of the bunch is seen to oscillate about the center axis with a greater amplitude than the head. The bottom panel shows the HEM_{11} mode amplitude at the end of the CWG module generated by the off-axis particles of the bunch [97]. The envelope of the HEM_{11} pulse correlates with the bunch offset in the top panel, where the signal at 1.02 ns is generated by the bunch at $z = 2$ m and is attenuated due to ohmic loss in the CWG.

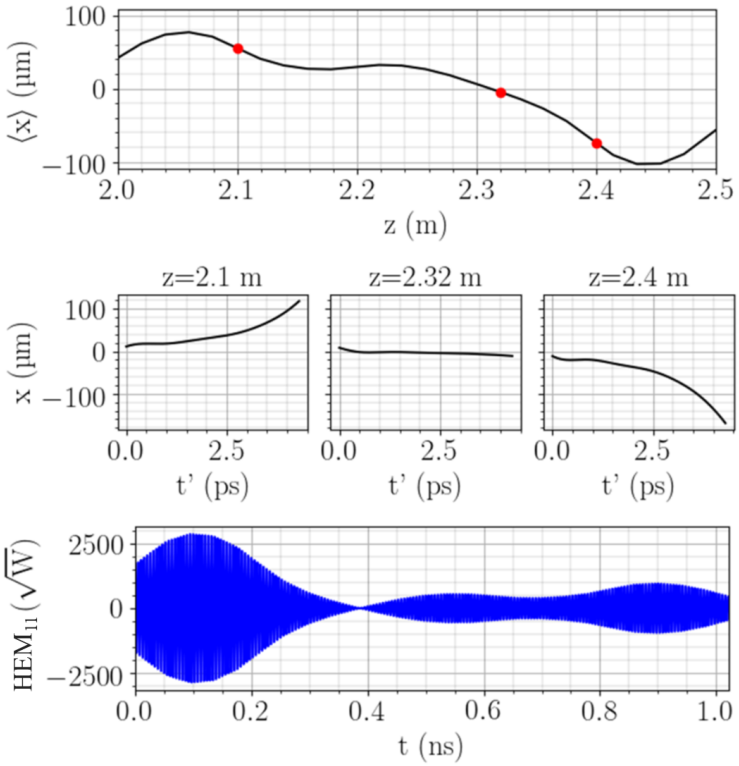

Figure 28. Bunch trajectory through the fifth accelerator module in the CWA showing the center of charge of the electron bunch (top panel), the bunch curvature at three locations in the CWG (middle panel), and the 190 GHz HEM_{11} mode at the end of the CWG module.

Repeating the HEM_{11} signal calculation for each CWG module in the CWA informs the total energy intercepted by each IOM as shown in figure 29. In this example, one quadrupole located in accelerator module 28 was misaligned by 5 µm, 6 µm, and 7 µm. The stable operating condition of the CWA is estimated to require quadrupole misalignment errors of less than 6 µm. Therefore, given the magnitude of the calculated IOM output energies, the IOMs are expected to inform about the unwanted beam oscillation in the accelerator long before the onset of any BBU instability.

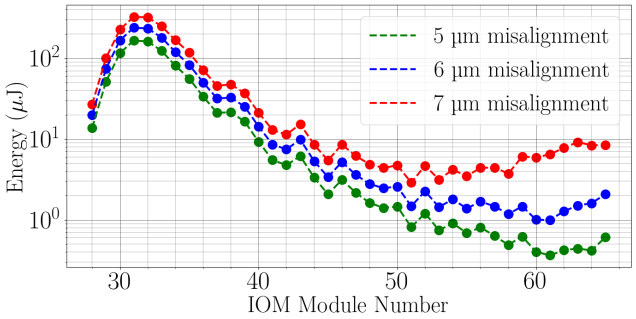

Figure 29. IOM output energies for one quadrupole's misalignments of 5 µm, 6 µm, and 7 µm, showing instability developing toward the end of the accelerator for the 7 µm misalignment case.

4.2.3 Diamond window design

The vacuum windows are needed to propagate electromagnetic waves (EMs) with high average power out of the structure. The window must have a minimal back reflection of the incoming EM wave and losses, maximizing the power it can safely extract. Therefore, the chemical vapor deposition (CVD) diamond was chosen as the window's material for its thermal and electrical properties. Currently, CVD diamond windows are used extensively in millimeter-wavelength gyrotrons operating at megawatt power levels [98, 99].

The design employs a double-window structure to protect the accelerator from a catastrophic failure of one of the windows. A larger diameter window is preferable for ease of manufacturing and assembly. Thus, the design consists of a rectangular-to-circular waveguide transition section leading to a circular waveguide with two circular diamond windows mounted in series. The rectangular waveguide is connected to one of the fundamental coupler's rectangular waveguide arms, which is under vacuum. The other side of the window section is at atmosphere, either radiating into a load via free space or directly into a waveguide load. A smooth taper provides good mode conversion from the rectangular fundamental waveguide mode TE_{10} to the circular mode TE_{11}. The length of the uptaper is 32 mm, with 5 mm of straight WR5.1 and 5 mm of straight circular waveguide on either side. Figure 30 shows the entire window structure.

The double-window design presents the potential issue of a standing wave developing between the two windows. This risk is mitigated by the spacing between the windows being at least a few wavelengths, chosen here as 24 mm, so any trapped standing waves would be attenuated. The space is also used for the vacuum gauge to control the integrity of the window assembly.

The window's thickness is determined by the EM wavelength at the operating frequency of 180 GHz within the material, dependent on its relative permittivity $\epsilon = 5.68$ for CVD diamond. The ideal thickness is an integer of the half wavelength, which at 180 GHz is 0.35 mm.

2025 JINST 20 P01023

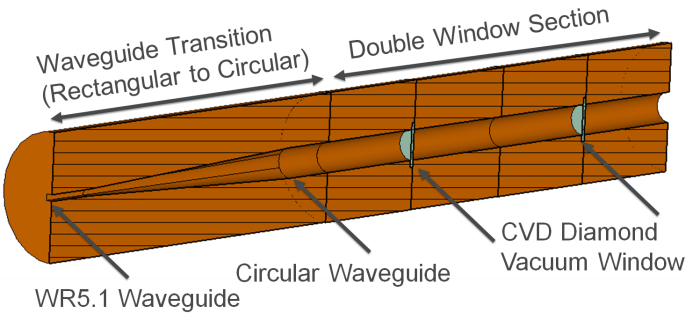

Figure 30. The diamond window assembly. On the left is the waveguide rectangular-to-circular transition. Two 4.4 mm-diameter diamond windows separated by 24 mm are in the center.

The diamond window design was simulated in CST Microwave Studio in the frequency domain, with the scattering parameter results shown in figure 31. At 180 GHz, the insertion loss S_{21} is −0.015 dB, which is the amount of signal that is not transmitted through the structure, either from conductive losses or reflection back. The return loss S_{11}, the amount of signal reflected back to the fundamental mode, is −25 dB, and the passband is 7.5 GHz. Note that this passband has two sharp dips on either end. These are resonance modes that occur within the diamond window and are a function of the window's material properties, thickness, and radius. These resonance modes are unavoidable and can only be shifted up or down in frequency by changing the thickness or radius of the window. During the design process these parameters were chosen to provide a large enough passband between resonances and ideally place the mode of operation in the center of the passband.

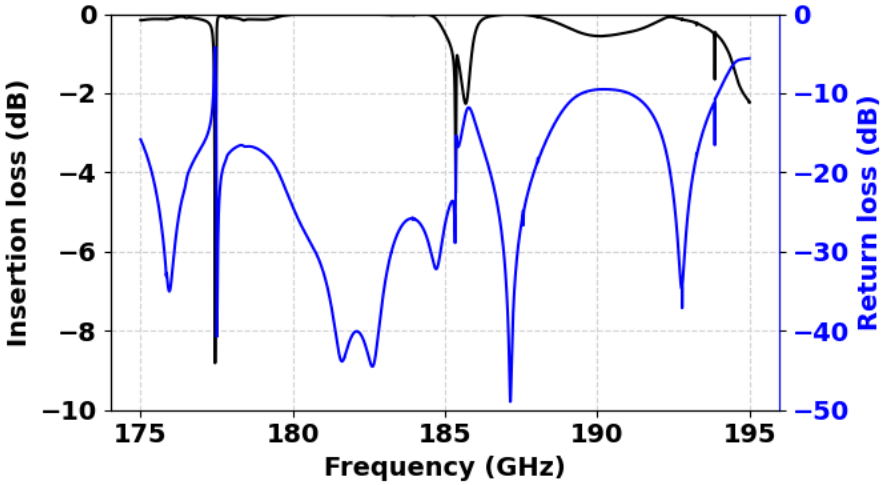

Figure 31. Insertion and return electromagnetic losses of the CVD diamond vacuum window assembly shown in figure 30, as calculated using CST Microwave Studio.

Simulations presented in table 4 show that a ±50 µm difference in thickness of diamond increases the insertion loss (S_{21}) at 180 GHz by 0.55 dB and 0.89 dB, respectively. Since ±50 µm would be equivalent to a half wavelength at 207 and 177 GHz, respectively, the degradation in performance with respect to a variance in the window's radius was not significant. More information is given in [100].

2025 JINST 20 P01023

Table 4. Tolerance analysis of the CVD diamond window's thickness and radius with the resulting insertion loss S_{21} at 180 GHz. In bold is the nominal insertion loss value −0.015 dB.

	S_{21} (dB)	Window Thickness		
	180 GHz	0.35 mm − 50 µm	0.35 mm	0.35 mm + 50 µm
Radius	2.2 mm − 50 µm	−0.70	−0.090	−0.64
	2.2 mm	−0.90	**−0.015**	−0.66
	2.2 mm + 50 µm	−0.815	−0.014	−0.77

4.2.4 Fabrication of the transition section

The mechanical design of the transition section is described in [101]. Figures 32 and 33 show its complex internal geometry.

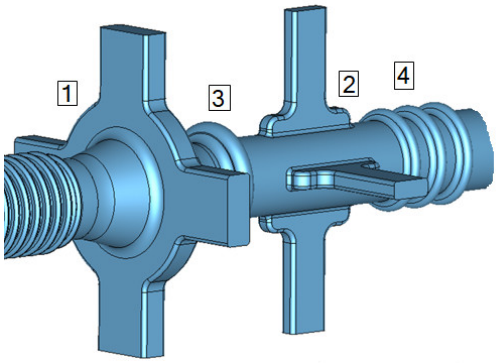

Figure 32. Geometry of the vacuum space for the transition section: (1) TM_{01} mode output coupler, (2) TE_{11} mode output coupler, (3) TM_{01} choke, and (4) TE_{11} choke. The structure's length is 15 mm, and it begins at the end of the corrugated waveguide. The beam moves from left to right.

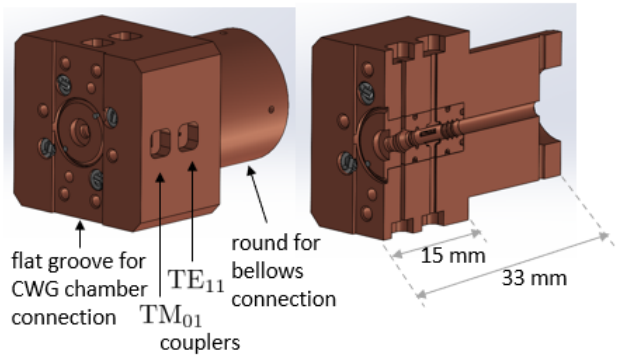

Figure 33. Mechanical design of the transition section showing a combined assembly of the electroformed core and copper core holder.

A specialized process was developed to manufacture a short yet multi-functional transition section [102]. Electroforming was utilized to create the internal geometry of the TS core. Micro-machining and electrical discharge machining (EDM) were used to make the copper core holder.

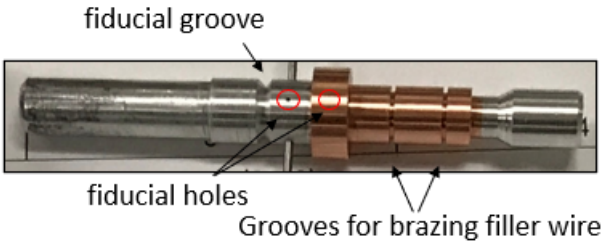

Figure 34. Aluminum mandrel with fiducial groove and fiducial holes, and a section with a negative profile of the internal TS geometry covered by electroformed copper. Copper is machined and has fiducial holes and grooves for brazing filler wire.

Achieving seamless integration between these two parts demands a high degree of positioning accuracy, necessitating the relocation of fiducial holes from the aluminum mandrel to the electroformed copper, as seen in figure 34. Presenting a unique challenge, precision EDM and wire-EDM must be applied to shape the rectangular waveguides inside the assembly with horizontal and vertical dimensions of 0.72 mm × 1.78 mm for the TM_{01} coupler and 1.10 mm × 0.45 mm for the TE_{11} coupler. A brass EDM wire with a diameter of 0.1 mm was used in both cases.

A single fully functional transition section was successfully fabricated and underwent comprehensive testing employing the electron beam at the ATF at Brookhaven National Laboratory, see section 5.1.2. Using specially designed electrodes, EDM was used for creating horn antennae at the waveguide ends for these tests.

4.3 Design of the quadrupole wiggler

As shown in figure 6, the row of alternating focusing (F) and defocusing (D) quadrupole magnets with a 3 mm bore diameter surround the corrugated waveguide. They are used to focus the electron beam and to facilitate the BNS damping. A study reported in [77] shows that using the quadrupole wiggler for suppression of BBU could be contra-productive if the rms value of the offsets of the quadrupole's magnetic centers relative to a common center line exceeds 1 µm in both x and y directions. In this case, the kicks to the electron beam trajectory produced by misaligned quadrupoles could initiate the BBU. Similarly, the yaw and pitch of the quadrupoles should be smaller than 200 microradians.

As stated in section 3, quadrupoles with different lengths are needed in the A-STAR to implement the adaptive focusing. Therefore, to demonstrate the feasibility of achieving the required alignment tolerances in all quadrupole wigglers, we initially constructed two 40 mm-long quadrupoles, which are close to the average length of all quadrupoles. Subsequently, we built four 25 mm-long quadrupoles using the same magnetic design.

4.3.1 Quadrupole wiggler magnetic design

The main objectives for the quadrupole's magnetic design were to attain the highest effective magnetic field gradient and have a space to house a chamber with the corrugated waveguide [103]. Therefore, we used an open space between magnetic poles in the horizontal plane for two NdFeB permanent magnets (PM) with opposing directions of magnetization to magnetize the four soft iron poles, and an open space between magnetic poles in the vertical plane for the chamber with corrugated waveguide, see figure 35.

2025 JINST 20 P01023

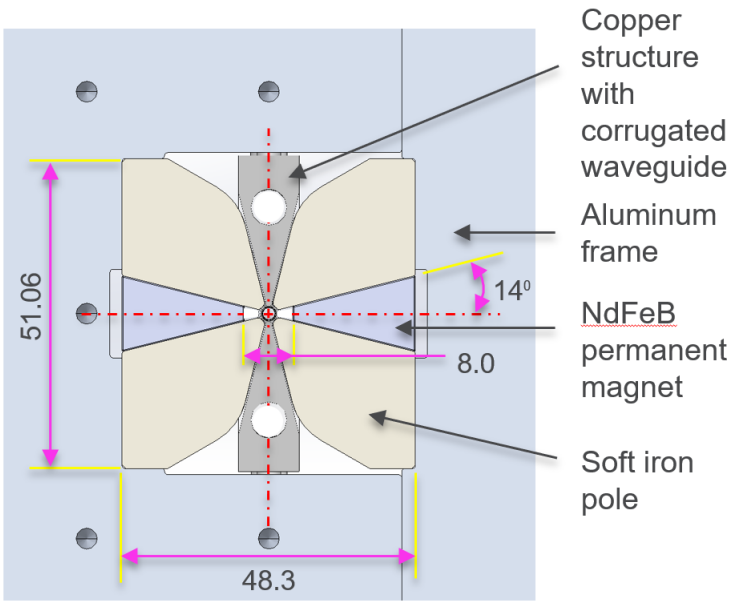

Figure 35. Cross section of the quadrupole's core. All dimensions are in millimeters.

Once the basic quadrupole configuration was defined, OPERA 3D [104] was used for further magnetic design optimization. It involved identifying the optimal cross-sectional dimensions of the PM blocks, the width of the pole's tip, the opening angle of the poles, the thickness of the pole roots, and the recess of the permanent magnet from the pole's tip. The optimization aimed to minimize parasitic fluxes, maximize useful flux within the bore region, and minimize magnetic flux losses between adjacent quadrupoles with opposite polarities. For the last purpose, the quadrupoles were moved slightly apart, and side magnets with the same cross-sectional geometry as the poles were installed into the gaps. They were magnetized in the direction orthogonal to the face planes of the poles. A small air gap was reserved for the correction of yaw and pitch misalignment errors.

Figure 36 shows the distribution of the magnetic field gradient along the quarter length of the quadrupole wiggler period calculated using 3.5 mm thick side magnets. The horizontal red dotted line shows the effective gradient $G_{\text{eff}} = 0.956$ T/mm as defined by the black curve and the effective quadrupole length $L_{\text{eff}} = 40.77$ mm. To define L_{eff}, we first found the maximum gradient on the middle of the quad $G_{\text{max}} = 0.959$ T/mm by fitting the calculated data on the middle of the

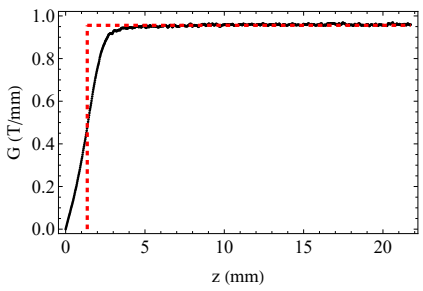

Figure 36. Magnetic field gradient along the half length of the quadrupole. See text for more details.

2025 JINST 20 P01023

quadrupole to a straight line, and then found a point on the z axis with the value of $G_{\max}/2$, as shown by the vertical red dotted line.

4.3.2 Quadrupole wiggler mechanical design

Here we describe the quadrupole wiggler mechanical design considering a 25 mm-long quadrupole. This is the shortest quadrupole in the A-STAR, and the one most constrained by the available space.

The mechanical design of the quadrupole wiggler shown in figure 37 comprises an optical table serving as a supporting platform, a rail system on which each fully assembled quadrupole is mounted, and an arrangement of individual quadrupoles. Quadrupoles are positioned on the rail system, slid into place, and securely clamped onto the rails.

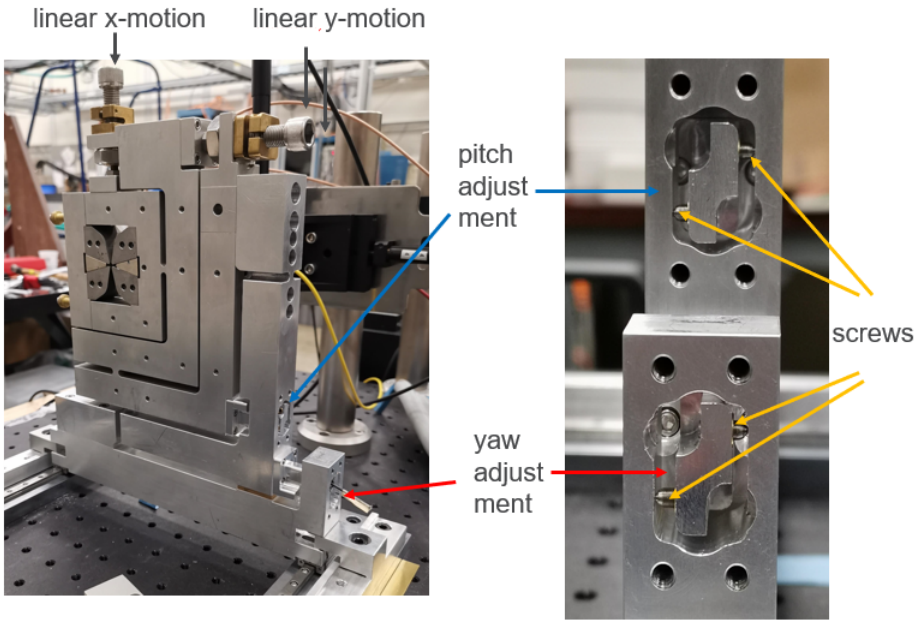

Figure 37. Quadrupole with adjustment mechanisms for x, y, pitch and yaw.

Flexure hinge mechanisms have been incorporated for the x and y linear motions to fulfill the requirements for sub-micron-level accuracy for the alignment of the quadrupole magnetic center. These mechanisms offer roll (Rz) motion with pivotal points on the x and y axes that in a limited range can be treated as pure x and y translations, see figure 37. The quarupole's roll is not critical for the system (in the range of several milliradians). The adjustment mechanisms employ simple differential screws, acting as two sine-arm driving stages.

Two extra flexure hinge mechanisms have been implemented for pitch (Rx) and yaw (Ry) adjustments. The pivotal points in this case are on the y and x axes, as shown in figure 37. In the case of the quadrupole wiggler located at the end of the accelerator, the main challenge is that all the adjustments must be accessed from the side within the 25 mm width of each quadrupole. Fortunately, access to each quadrupole is possible from the side to adjust ultra-fine thread, ball-point setscrews in the z direction. This significantly simplifies the design and addresses the pitch (Rx) and yaw (Ry) motion adjustments by using two setscrews per motion, one in the positive z direction and one in the negative z direction, for both Rx and Ry adjustments respectively, as shown in the right part of figure 37.

2025 JINST 20 P01023

After the quadrupole wiggler has been fully assembled and preliminary aligned, the vacuum chamber has to be installed. Hence, each quadrupole must have the capability to be split into halves and reassembled after the installation of the vacuum chamber, see figure 38.

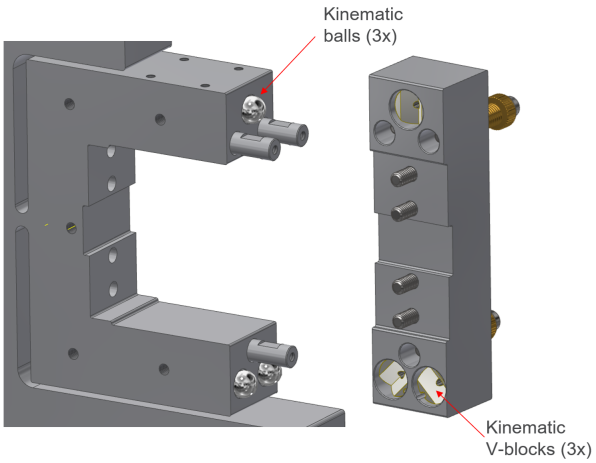

Figure 38. Kinematic system with three sets of balls and V-blocks for repositioning of the half quadrupole.

5 Test of A-STAR components

The comprehensive tests of key components of the A-STAR accelerator module were performed. They included characterization of the CWG and the TS with the electron beam, and bench measurements and alignment of the quadrupole wiggler prototype.

5.1 Test with the electron beam

All tests with the electron beam were performed at Brookhaven National Laboratory's Accelerator Test Facility (ATF) [105, 106] using an electron beam with parameters listed in table 5. The electron bunch length ℓ_b was controlled by the width of a vertical slit in the so-called energy collimator located inside of a dog-leg-type magnetic lattice at a location with a large horizontal dispersion function. The slit passes electrons with a predominantly flat-top charge distribution and a fixed central energy that is independent of fluctuations in central energy of the incoming electron bunch. The slit width and the RF phase in the linac were used to control the bunch charge passed through the slit. Figure 39 shows the electron beam image at the energy collimator screen with the slit located in the center.

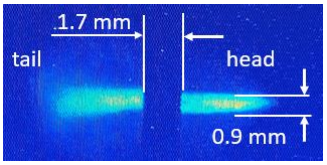

Figure 39. The electron beam image at the energy collimator screen with a slit in the middle. The screen cuts off the bunch tails, transmits electrons only within a fixed energy range, and produces an electron bunch after the collimator with a predominantly flat-top charge distribution. The head of the bunch has a lower energy than the tail due to the energy chirp.

2025 JINST 20 P01023

Three sets of the electron beam parameters used in the experiments are given in table 5.

Table 5. Electron beam parameters at ATF. NA stands for not applicable.

Parameter	Value 1	Value 2	Value 3	Unit
Beam energy	55	55	55	MeV
Bunch charge	150	130/170	10–40	pC
Charge distribution	flat top	flat top	flat top	
Bunch length, ℓ_b/c	1.5	5	1–2	ps
RMS slice energy spread	NA	65	NA	keV

A schematic of the experimental setup shown in figure 40 is generic for all tests performed using the electron beam. After passing the dog-leg-type magnetic lattice (12) with the energy collimator (13), the electron bunch enters the experimental chamber from the right and passes through the device under test (DUT). It exits the experimental chamber and passes the spectrometer magnet (15) as it proceeds to the Faraday cup (16) inside the beam dump enclosure (17). Other components include two retractable YAG-screen-based beam position monitors (7), an off-axis parabolic mirror (8), a polymethylpentene (TPX) window (9) with close to a 100% transmission efficiency of sub-terahertz and visible light, a Michelson interferometer (10), a liquid helium bolometer (11), a slit (19), a diagnostic screen (18), and a helium-neon alignment laser (14). The specific DUT shown in figure 40 contains the CWG (1), adapter (3), TS (2), and the end piece (6). It is discussed in section 5.1.2.

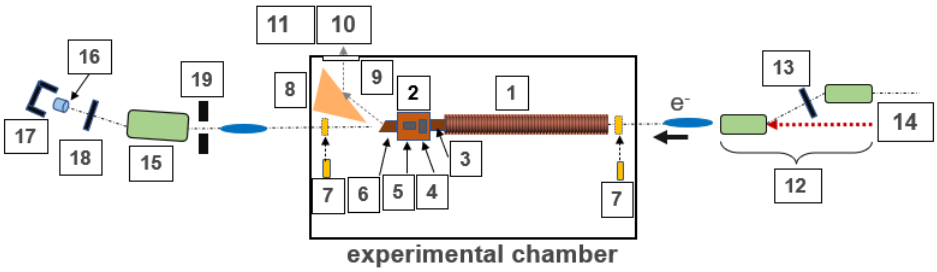

Figure 40. Schematic of the experiment showing the device under test and other principle components of the experiment. See the text for an explanation of the components.

5.1.1 Corrugated waveguide

The first DUT consisted of a set of three CWGs with lengths of L_c = 96 mm, 74 mm, and 34 mm mounted on an aluminum holder attached to the horizontal translation stage, see figure 41.

In the first set of experiments, we used the electron bunch with parameters from the second column in table 5 and the interferometer to determine the frequencies of the monopole, dipole, and quadrupole modes of the sub-THz Čerenkov radiation produced by this bunch passing through the CWGs [91]. Using the shortest CWG with L_c = 34 mm, we measured the duration of the radiation pulse Δt and calculated v_g with which the monopole TM_{01} mode propagates downstream of the CWG from this equation

$$\Delta t = L_c \left(\frac{1}{v_g} - \frac{1}{v} \right), \tag{5.1}$$

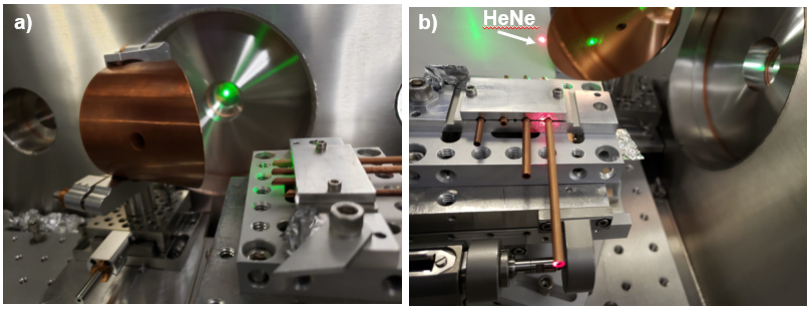

Figure 41. A setup of the experiment with corrugated waveguides: (a) side view showing the CWGs, a back side of the off-axis parabolic mirror (8), the TPX window (9) illuminated by an alignment green laser, (b) front view demonstrating alignment of the CWGs using HeNe laser (14). The numbers are consistent with ones given in figure 40.

where $v = c\sqrt{1 - 1/\gamma^2}$ is the electron bunch velocity and γ is the relativistic factor. Figure 42(a) shows the interferogram and the best fit obtained using the monopole mode frequency of $f_m = 186\,\text{GHz}$ deduced from the Fourier transform of the interferogram and $v_g = 0.55c$ deduced from eq. (5.1) while adjusting Δt to fit the rising and falling interferogram 'shoulders'. The design value is $0.57c$.

Figure 42(b) shows the Fourier transform of the interferogram obtained using the CWG with $L_c = 96\,\text{mm}$. The absence of high-order monopole modes in the spectrum validates the important design goal for the corrugated waveguide. Prior to this measurement we carefully adjusted the electron beam trajectory in the vertical and horizontal planes to the center of the CWG to minimize the dipole and quadrupole modes of Čerenkov radiation driven by the beam offset. The measured frequency of the TM_{01} mode $f_m = 192 \pm 5\,\text{GHz}$ falls within the acceptable fabrication error margin defined by the respective 3 dB bandwidths of the TM_{01} mode coupler.

In the second set of measurements, we used the electron bunch parameters from the third column in table 5 with the flat charge distribution

$$q(s) \simeq \frac{q_0}{\ell_b}\left(\theta(s) - \theta(s - \ell_b)\right), \tag{5.2}$$

where $\theta(s)$ is the unit step function. The bunch length was comparable to the wavelength of the monopole TM_{01}. Therefore, the wakefield acting on the bunch electrons was expected to produce sinusoidal-like energy modulation along the bunch covering regions with decelerated and accelerated electrons [91],

$$\Delta\mathcal{E}(s) = -2\kappa_{\|} L_c \frac{q_0}{k\ell_b} \sin(ks), \quad s \le l_b. \tag{5.3}$$

We measured this energy modulation and compared it with the calculation. Initially, we calibrated the spectrometer magnet (15) (see, figure 40) using the diagnostic screen (18), ran the electron bunch in the linac on crest of the linac's radio frequency (RF) accelerating field and determined, though preliminary, the uncorrelated (slice) energy spread σ_E using the beam image on the diagnostics screen (18). The slit (19) located after the experimental chamber was used in this experiment to reduce the bunch charge and the coherent synchrotron radiation in the spectrometer magnet. Next, we recorded the image shown in figure 43(d) after the electron bunch propagated a 102 mm-long copper tube without corrugations with a 2.1 mm ID. After that, we reproduced figure 43(d) in simulations,

2025 JINST 20 P01023

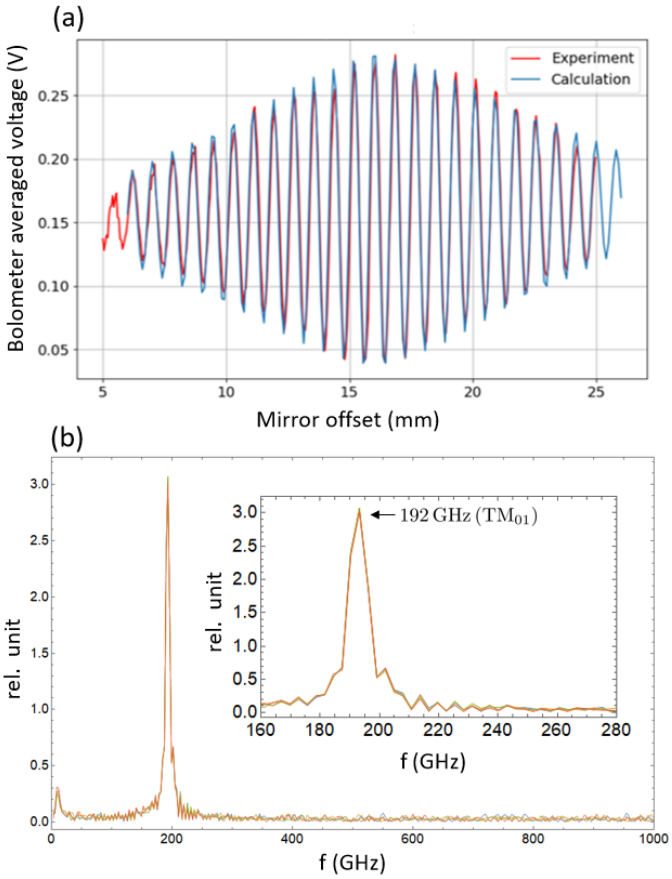

Figure 42. (a) The interferogram obtained when the electron bunch propagated through the CWG with the length L_c = 34 mm. (b) The spectrum of the radiation emitted when the electron bunch propagated through the CWG with the length L_c = 96 mm.

fitting the image by using as the main parameter the RF phase ϕ_{RF} for the electron bunch acceleration in the linac because it defines the energy chirp in the electron bunch, and also using σ_E as the secondary parameter probing small deviations from the predetermined value. The result is shown in figure 43(b). The fitted values are σ_E = 65 keV and ϕ_{RF} = 6.0°. Using these values, we modeled the electron distribution in the longitudinal phase space and plotted it in figure 43(a). From that distribution we obtained the histogram of electron energy distribution and plotted it in figure 43(c).

After completing the above-described baseline measurements, we measured the impact of the wakefield on the electron bunch propagating the CWG with L_c = 74 mm [91]. Figure 43(h) shows an electron bunch image measured at the diagnostic screen. Using eq. (5.3) and the above-defined σ_E and ϕ_{RF}, we modeled the electron distribution in the longitudinal phase space (see figure 43(e)), the electron bunch image at the diagnostic screen (see figure 43(f)), and the electron energy distribution (see figure 43(g)). The appearance of the two lobes on the sides that are absent in figure 43(d) clearly indicates the impact of the wakefield. Indeed, because the bunch length is comparable to the period of the wakefield oscillations of 5.6 ps, observing both decelerated and accelerated electrons is expected as confirmed by the results of the calculation shown in figure 43(e) and figure 43(g), and by the measurement in figure 43(h). We note that figure 43(f) closely resembles the measurement. A similar observation in the experiments with the corrugated waveguide was reported previously in [107].

2025 JINST 20 P01023

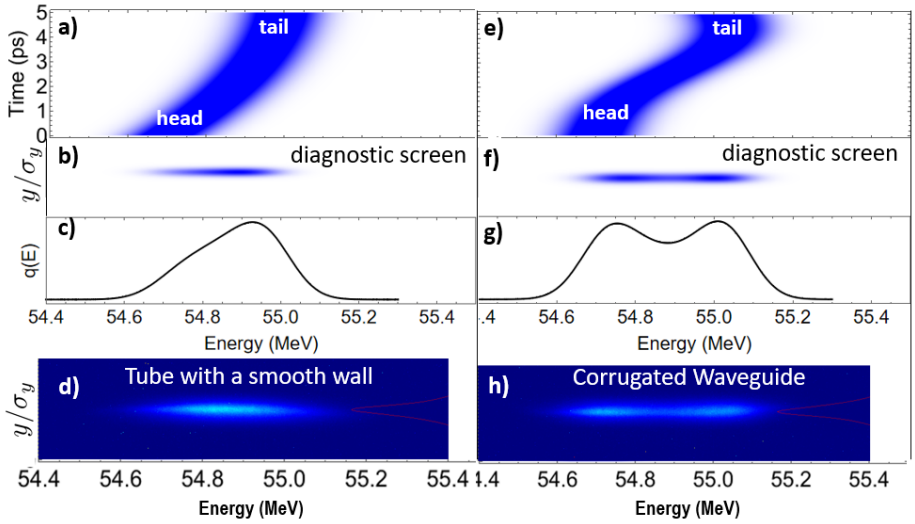

Figure 43. Comparing measurements and simulations for the cases of the electron bunch propagating the tube with smooth wall (left column of plots) and the corrugated waveguide with L_c = 74 mm (right column of plots). Plots (a) and (e) show the simulated distribution of electrons in the longitudinal phase space using energy on the horizontal axis and time on the vertical axis. Plots (b) and (f) show the simulated bunch image on the diagnostic screen using energy on the horizontal axis and the vertical coordinate y normalized on the rms vertical size σ_y on the vertical axis. Plots (c) and (g) show the simulated bunch energy distribution using energy on the horizontal axis and the charge in arbitrary units on the vertical axis. Plots (d) and (h) are similar to plots (b) and (f) and show the measured bunch image on the diagnostic screen using energy on the horizontal axis and the normalized vertical coordinate on the vertical axis.

To summarize, in the beam test of the CWG, we verified the absence of the higher-order longitudinal modes in the wakefield, measured the frequency of the fundamental longitudinal wakefield mode, measured the group velocity of this mode, and measured the impact of the wakefield on the energy modulation of the electrons. All results agree with the calculations within the acceptable margin of fabrication errors.

5.1.2 Prototype of the accelerator module

We fabricated the 300 mm-long CWG (1) and the transition section (2) with a short 2 mm internal diameter adapter pipe between them (3) and installed it for the beam test into ATF's experimental chamber, see figure 44. This DUT closely resembled the 500 mm-long vacuum assembly of the proposed A-STAR accelerator module and was the longest DUT that could fit inside the chamber. In this experiment, the CWG and the TS were not brazed to facilitate testing the same TS with two different CWGs. Occasionally, the end piece (6), consisting of a short copper pipe with a 2 mm internal diameter and an end cut at a 45° angle, was attached to the assembly to extract radiation propagated past the TM_{01} and TE_{11} couplers in the TS. The DUT was mounted on the assembly of two Zaber linear stages (20): model LSM050A-V2T4 for horizontal movement and model VSR40A-V2T4 for vertical movement. The vendor-specified error over the short movement is 5 µm.

We tested this prototype accelerator module using an electron beam with parameters listed in the forth column of table 5. The primary objective of the electron beam test was to validate the TS performance against the functionality designated by the design. Initially, we confirmed the production of the expected Čerenkov radiation by the electron bunch as it traversed the 300 mm-long

2025 JINST 20 P01023

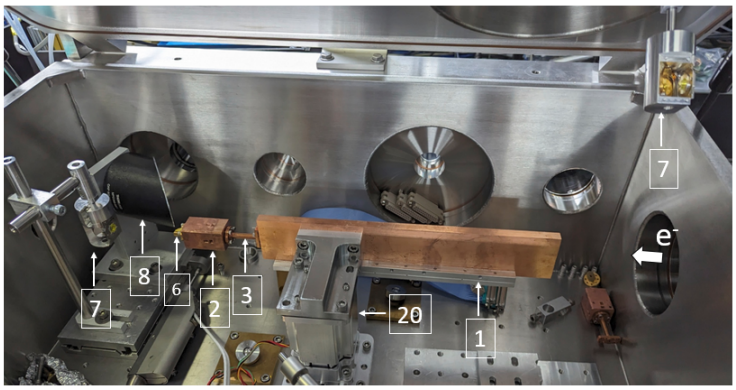

Figure 44. Photo shows the CWG (1), TS (2), adapter (3), and the end piece (6) installed in the experimental chamber. The experimental setup also includes the off-axis parabolic mirror (8) and two BPMs (7). The DUT was mounted on the assembly of two Zaber linear stages (20). The direction of the electron beam motion in this view is from the right to the left.

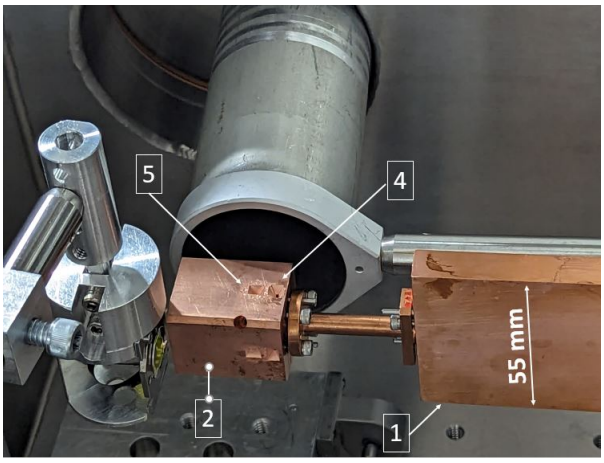

Figure 45. Photo of the TS installed facing the TPX window. The CWG with a strongback support (1), TS (2), horn antenna of the TM_{01} mode coupler (4), and horn antenna of the TE_{11} mode coupler (5).

CWG [102]. Subsequently, the TS was positioned opposite the TPX window, as depicted in figure 45, and an interferometer was employed to simultaneously assess the spectrum of the two overlapping sub-terahertz waves from the TM_{01} and the TE_{11} couplers emitted from the two horns located on the side of the TS facing the window. To prevent stray waves from the other TS horns from entering the window, a 2-inch diameter aluminum tube was utilized.

Figure 46 presents two Čerenkov radiation spectra measurements. In these and all subsequent measurements, the beam propagated through the CWG with the 150 µm offset from the center. This offset was achieved by moving the DUT downwards using the vertical linear stage. The first measurement was conducted without using the wire grid polarizer and the second measurement was carried out with the polarizer installed behind the TPX window and in front of the interferometer. The polarizer was oriented vertically and was expected to completely attenuate the horizontally polarized sub-terahertz wave originating from the TM_{01} mode coupler antenna and to leave the vertically polarized sub-terahertz wave from the TE_{11} coupler unaffected. However, in practice, a minor portion of the TM_{01} mode reached the detector due to polarization-altering reflections within the aluminum

2025 JINST 20 P01023

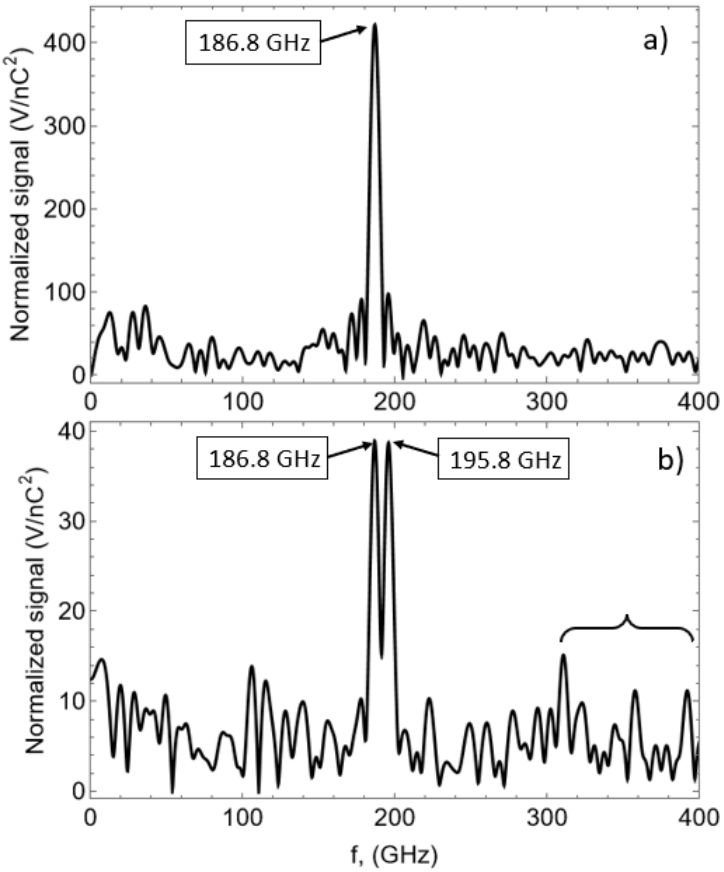

Figure 46. Spectra measured (a) without and (b) with the polarizer. The high-frequency peaks delineated by a figure bracket are due to a beam offset at the location of the TE_{11} mode coupler.

tube. The measurements indicate that the ratio of the total energy contained in the sub-terahertz HEM_{11} mode to that of the TM_{01} mode is 0.093 ± 0.006. Using eq. (3) and table 1 from [97] and the vertical beam offset of 150 µm, we calculated 0.091. This calculation considered that TM_{01} mode pulse energy is divided between four ports in the TM_{01} mode coupler, and HEM_{11} mode pulse energy is divided between two ports in the TE_{11} mode coupler. This agreement between measurement and theory is noteworthy, considering potential uncertainties in defining the reference trajectory of the electron beam.

The measured frequencies were 186.8 ± 1.6 GHz for the TM_{01} mode of Čerenkov radiation and 195.8 ± 1.6 GHz for the HEM_{11} mode of Čerenkov radiation. It is also worth noting that several small amplitude peaks at the high-frequency end of the spectrum seen in figure 46(b) are due to the beam offset at the location of the TE_{11} coupler predicted in [97].

For validation of the TS performance with electron beam, the bolometer was installed behind the TPX window and the polarizer. During the first round of measurements, the TS was positioned in line with the TPX window, as seen in figure 45. The bolometer was used to measure the energy of the sub-terahertz wave pulses emitted by the TS horn antennae. The polarizer orientation was alternated between vertical and horizontal, enabling transmission of the light with each polarization direction to separately isolate the sub-terahertz radiation produced by the TM_{01} coupler and the TE_{11} coupler.

For the second round of measurements, the experimental setup was modified to that depicted in figure 44 to measure the sub-terahertz radiation that did not couple to either the TM_{01} or TE_{11} couplers.

2025 JINST 20 P01023

The end piece (6) was attached to the TS, and the off-axis parabolic mirror (8) was installed to redirect the sub-terahertz waves emitted from the end piece to the bolometer. The 45° cut at the end of the end piece was used to direct the sub-terahertz waves to the mirror [97, 108]. Meanwhile, the transition radiation due to the electron bunch exiting the end piece propagated forward, circumventing the mirror. The bolometer was used to measure the energy of the sub-terahertz wave pulses emitted by the end piece and transmitted by the polarizer oriented either vertically or horizontally, as described above.

All the above-described measurements were performed two times using the same transition section and two unique corrugated waveguides. The vertical beam offset from the reference was held at $\sim 150 \pm 40\,\mu$m.

The results of the measurements using the output from the horn antennae of the TM_{01} or TE_{11} couplers and the end piece are given in table 6. Since the peak voltage of the bolometer signal is proportional to the energy of the sub-terahertz wave pulse, and since this energy scales quadratically with the electron bunch charge, the table shows the ratio of the peak voltage of the bolometer signal measured by the oscilloscope in Volts to the square of the electron bunch charge in nano coulombs measured by the Faraday cup, i.e., V/nC^2. Each entry in the table shows the mean value of 50 to 90 measurements and a standard deviation. The uncertainties of the standard deviations due to a limited number of measurements are in the range of 7.5–10%. The fluctuations were mainly caused by jitters in the RF phase and amplitude in the ATF linac and the laser pulse timing in the photocathode gun. The difference in magnitude of the signal from the two experimental CWGs is likely due to an improved manufacturing and assembly process, which reduced the number of brazing cycles and created a more controllable machined joint to improve the integrity of the corrugated geometry.

Table 6. Measurement results, all entries have dimension V/nC^2.

Name	horn antenna		end piece	
	TM_{01}	TE_{11}		
Polarization	horizontal	vertical	horizontal	vertical
CWG_1	2419 ± 493	707 ± 125	212 ± 14	151 ± 17
CWG_2	4282 ± 518	1834 ± 223	735 ± 250	848 ± 263

Considering that the TM_{01} mode pulse energy is divided between four TM_{01} coupler's horn antennae, and HEM_{11} mode pulse energy is mainly equally divided between two TE_{11} coupler's horn antennae, we find analyzing this data that the TM_{01} coupler captures (97.8 ± 0.5)% of the TM_{01} mode of Čerenkov radiation and the TE_{11} coupler captures (89.3 ± 2.2)% of the HEM_{11} mode of Čerenkov radiation in the case of the CWG_1. The corresponding numbers in the case of the CWG_2 are (95.7 ± 1.5)% and (76.9 ± 7.7)%. This is compared with respect to extraction efficiencies of 99.1% and 73.4% calculated in [97]. Linac tuning and realignment of the DUT were performed after each new installation to minimize the systematic error.

Based on the above measurements, we concluded that the TS effectively fulfills the primary functions of its design [102].

5.2 Magnetic measurements of the quadrupole wiggler

Measurements of the magnetic field of individual quadrupoles and the quadrupole wiggler were made using the pulsed wire method [109–111] since this method requires only a small space inside the

2025 JINST 20 P01023

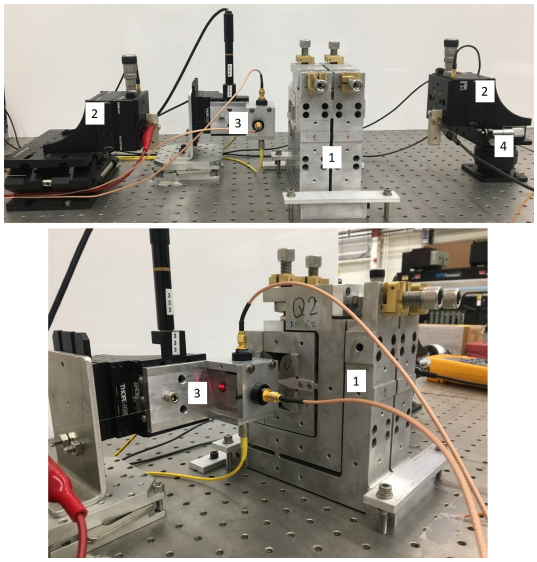

Figure 47. Pulsed wire measurement bench setup: (1) two quadrupoles representing one period of the quadrupole wiggler, (2) piezo stages, (3) laser-photodiode pairs, (4) one of the two linear stages for tensioning the wire.

quadrupoles to place a tensioned wire. A pulsed wire measurement bench, shown in figure 47, was built to characterize the quadrupole wiggler prototype [112]. The photos also show two 40 mm-long quadrupoles fabricated for initial tests.

During the measurement of an individual quadrupole, manual micrometer adjusters were used on the horizontal and vertical piezo stages to get the wire close to the center of the quadrupole. Following this, the wire was moved in increments of 0.5 µm using piezo stages to determine the sensitivity of the alignment method to the magnetic field integral. Displayed in figure 48 is the position of the wire with respect to the magnetic center of the quadrupole in the x and y directions deduced from the magnetic measurement in correspondence to the movement of the wire by the piezo stages. The linear fit to the data shows a remarkable one-to-one correspondence between the driven offset of the wire and the measured offset. The integrated gradient measured in table 7 is

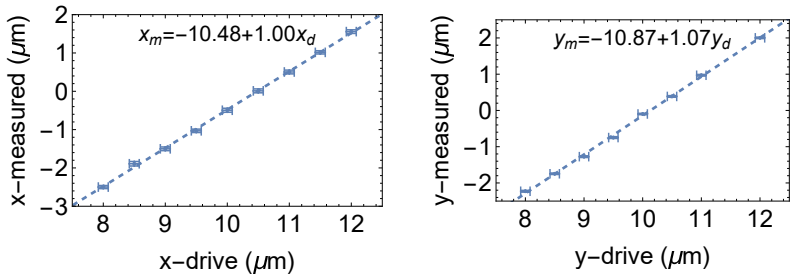

Figure 48. The wire scan measurements. The horizontal axes show the horizontal and vertical positions of the piezo stages "x-drive" and "y-drive". The vertical axes show the measured horizontal and vertical positions of the wire "x-measured" and "y-measured". The linear fit of the measured values is also shown as a function of the drive values. The horizontal error bar is determined by the error in the location of the piezo stages, and the vertical error bars are determined from the spread in the measured data.

2025 JINST 20 P01023

Table 7. Measured integrated gradient.

	Integrated gradient (T)	Standard deviation (T)
Horizontal	31.28	1.22
Vertical	30.97	2.33

one of the 40 mm-long quadrupoles. The numbers are close to the predicted integrated gradient of 30.25 T from magnetic modeling of the quadrupole design.

The goal of the quadrupole wiggler alignment is to align the central magnetic axes of all quadrupoles to the pulsed wire with a precision of less than 1 µm in both x and y and directions and to keep the yaw and pitch of the quadrupoles smaller than 200 microradians. These difficult requirements are essential for keeping BBU under control [77].

Figure 49 shows the result of alignment of two 40 mm-long quadrupoles. The slopes seen in both plots are believed to be mainly due to the angles between the quadrupole axes and the wire. Since 40 mm-long quadrupoles were fabricated without mechanical assemblies for angular alignment, the plots exemplify the best effort in manual angular alignment.

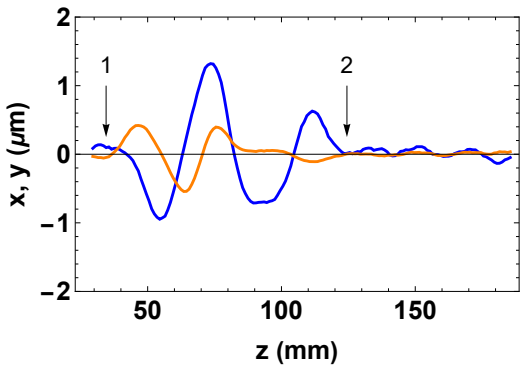

Figure 49. Illustration of the alignment of the second quadrupole in x (blue curve) and y (orange curve) to the wire whose position was previously aligned to the magnetic center of the first quadrupole. The first arrow shows the beginning of the first quadrupole, and the second arrow shows the end of the second quadrupole.

We fabricated four 25 mm-long quadrupoles that are equipped with the screw-driven angular adjustment mechanism described in section 4.3.2, assembled a two-period quadrupole wiggler on the high-precision girders that are parallel to each other, and aligned the wire parallel to the girders. The assembled wiggler prototype is shown in figure 50.

This quadrupole wiggler was measured with the pulsed wire, the misalignment information was derived from the measurements, and the corresponding adjustment was applied. After several iterations, no further reduction to the pulsed wire signals could be made, and the quadrupole wiggler was considered well-aligned. The final quadrupole magnetic axis offset from the wire derived from the first field integral measurement are shown in figure 51. The magnetic center offsets in each quadrupole averaged over the quadrupole length are less than 1 µm, and the yaw and pitch rotations of each quadrupole are less than 200 µrad.

2025 JINST 20 P01023

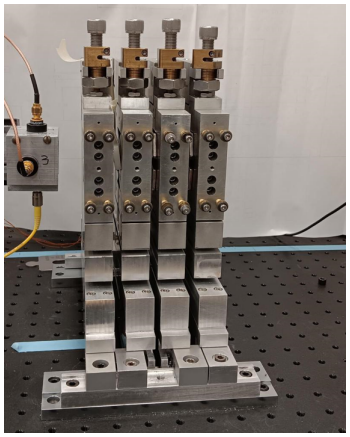

Figure 50. The quadrupole wiggler prototype consisting of four 25 mm-long quadrupoles forming two wiggler periods.

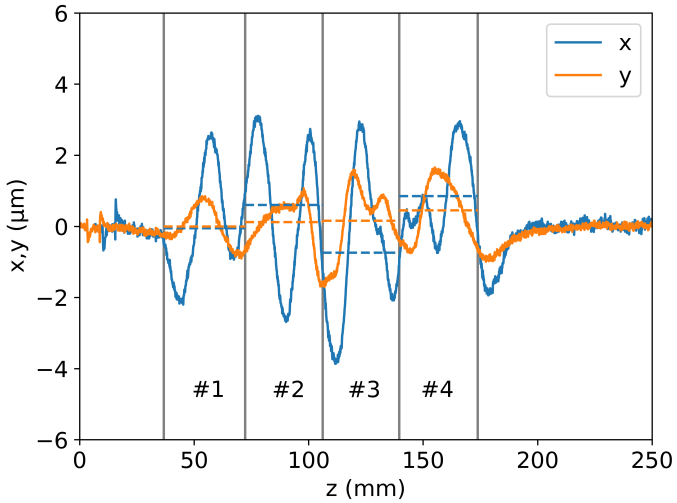

Figure 51. The final state of the alignment. The labels at the bottom of the panel indicate the serial numbers of the quadrupoles, which are separated by vertical lines. The dashed blue and orange lines indicate the averaged horizontal and vertical quadrupole magnetic center offsets.

After initial alignment, the prototype quadrupole wiggler array underwent a series of twelve pulsed wire measurements over six days. The recorded ambient temperature shows a variation range of 0.7°C, which is within the 1°C temperature regulation range in the measurement laboratory.

Throughout the observed duration, neither x displacement nor yaw rotation was observed. However, there was a variation with the amplitude of 2.5 µm in the y positions of the quadrupoles. It has been observed that the variation in the y position of each quadrupole exhibits a correlation with ambient temperature changes, as delineated in figure 52. The quantified linear correlation coefficients for each quadrupole span from 4.13 µm/°C to 4.37 µm/°C. Temperature is the dominant factor affecting the quadrupole center drift in y. This implies that a tighter requirement for environmental temperature stability during measurements and operation must be imposed.

To summarize, achieving a target accuracy in the alignment of two prototype quadrupole wigglers has been demonstrated. The sensitivity of the quadrupole wiggler alignment to the ambient temperature has been quantified.

2025 JINST 20 P01023

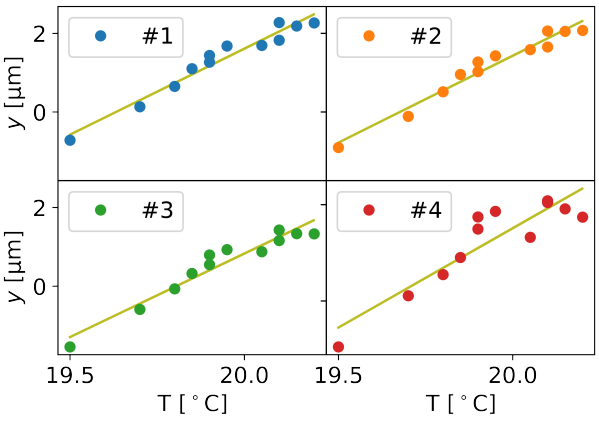

Figure 52. Variations in the y-centers with temperature for each quadrupole are depicted. Dots denote the data points, and their corresponding linear fits are illustrated with solid lines. The linear coefficients corresponding to quadrupoles #1 through #4 are 4.37, 4.42, 4.24, and 4.13 µm/°C, respectively.

6 Preliminary XFEL design

6.1 Undulator design

Figure 53 shows a force-neutral adjustable phase undulator (FNAPU) [61] that will be used in most of A-STAR's XFELs. It has a small size — 135 mm × 135 mm × 1890 mm — and requires only 0.3 mm of air space between the vacuum chamber and the magnetic structure. With a 2 mm beam-stay-clear aperture in the CWA, we can accommodate an undulator vacuum chamber with an inside diameter of 2.0 mm and an outside diameter of 2.4 mm, and use a FNAPU with a fixed gap of 2.7 mm. This is a 26% smaller gap than the smallest gap of an undulator with a vertically adjustable gap, which requires at least a 1 mm air space.

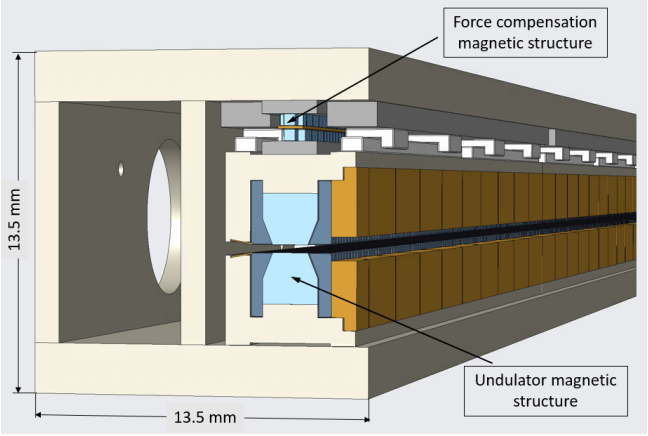

Figure 53. Force-neutral adjustable phase undulator with vertical gap orientation.

The undulator consists of a primary magnetic structure and a same-period secondary magnetic structure. The secondary structure is used to neutralize the magnetic forces of the primary structure. It uses a smaller gap between the two magnet rows and weaker magnets than the primary structure since the magnetic field between the two magnet rows depends on the gap exponentially, and the force due to the magnetic field scales quadratically with the field. The primary structure contains

permendur poles magnetized by the NdFeB permanent magnets. The secondary structure is made only from permanent magnets. The lower magnet rows of the FNAPU's primary and secondary structures are permanently attached to the supporting frames. The upper magnet rows of the FNAPU's primary and secondary structures are mechanically coupled and move together along the undulator axis when adjustment of the undulator parameter K is performed.

To reach a maximum undulator parameter $K \simeq 1.5$, undulator design parameters have been optimized as shown in table 8. While the prime magnetic structure uses strong NdFeB permanent magnets, grade N42SH, the secondary force compensation structure uses weak inexpensive NdFeB magnets, grade N42, with x, y, z dimensions of 20 mm, 5 mm, and 5 mm, respectively.

Table 8. FNAPU parameters.

Parameter	**Value**	**Units**
Gap	2.7	mm
Period length	12.6	mm
Undulator length	1.89	m
Pole material	Vanadium permendur	
Magnet material	NdFeB, grade N42SH	
Pole x, y, z dimensions	22, 20, 2.6	mm
Magnet x, y, z dimensions	32, 25, 3.7	mm
Magnet y recess	0.1	mm
Peak magnetic field	1.34	T
Undulator parameter K	1.57	

The FNAPU can be assembled with either vertical or horizontal orientation of the magnetic structures to produce light with either horizontal or vertical polarization. Several FNAPUs can easily fit in one tunnel.

As a proof of principle, a 27 mm period length FNAPU was built at the Advanced Photon Source using the legacy magnetic structure and characterized with the magnetic measurements [62], see figure 54. Measurements demonstrated that this FNAPU achieved the expected performance.

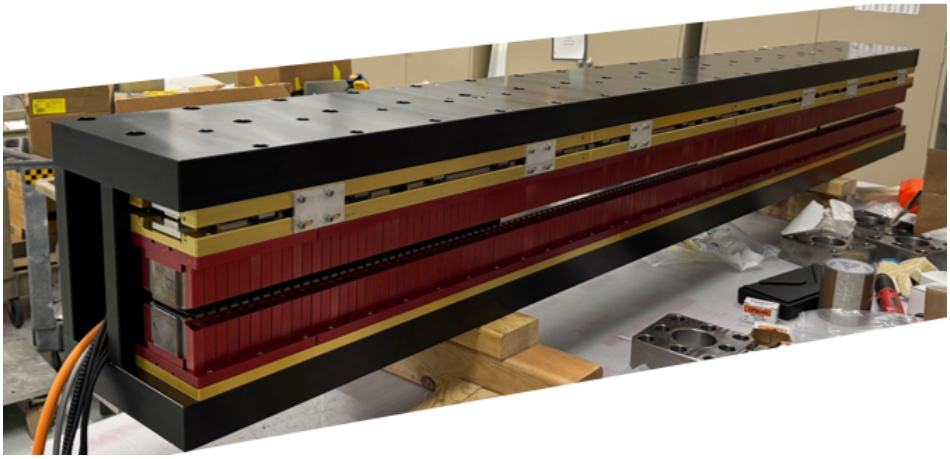

Figure 54. 2.4-meter-long FNAPU with a 27 mm period length. The height is 297 mm and the width is 248 mm.

2025 JINST 20 P01023

6.2 Preliminary design of the X-ray free-electron laser

Here we present results of simulations demonstrating the feasibility of generating X-ray photons with energies of 6.7 keV and 10.2 keV using a 4.5 GeV witness electron beam and the FNAPU undulator with $K = 1.57$ and $K = 1$, correspondingly. These photon energies represent the corners of the top line in figure 2. The simulations were performed using the Genesis code [113]. In our opinion, proof of feasibility for such an XFEL also proves that other XFELs generating lower energy photons shown in figure 2 can also be built.

The analytical model developed by Xie [114] was used to determine the average beta-function in the XFEL, β_u, that corresponds to the shortest gain length. We conducted two sets of calculations using a witness electron beam with target parameters shown in table 9. They are comparable to the parameters of the electron beam at the Swiss FEL [115]. In the first calculation, an undulator with $K = 1$ was used, resulting in the generation of 10.2 keV photons in the XFEL. In the second calculation, the undulator parameter was increased to its maximum value of $K = 1.57$, resulting in the XFEL producing 6.7 keV photons. The results of both calculations are presented in figure 55.

Table 9. Witness beam parameters.

Parameter	Value	Unit
Energy	4.5	GeV
Energy spread, $\sigma_{\mathcal{E}w}$	0.9	MeV
Norm. emittance, hor/ver	0.25/0.25	µm
Charge	0.1	nC
Peak current	3	kA
Distribution	flat top	
Bunch length	10	µm

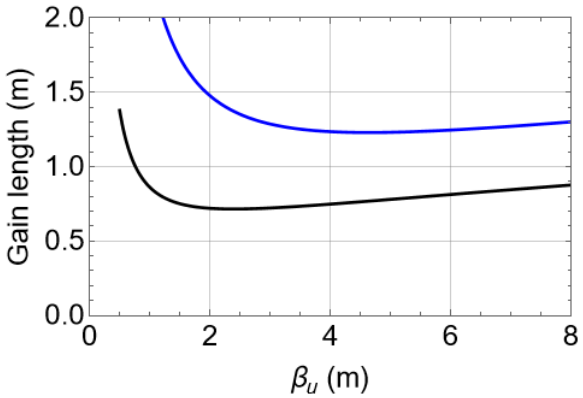

Figure 55. Gain length versus the average beta-function in the FEL. The case of 10.2 keV photon energy is shown in blue color, and the case of the 6.7 keV photon energy is shown in black color.

With all other parameters beam equal, the use of a larger β_u supports the XFEL lattice with the longer undulator sections. Therefore, based on findings shown in figure 55, we designed the undulator lattice with $\beta_u = 6.5$ m. It is a FODO-type lattice where the long drifts are occupied by the 1.89 m-long FNAPU undulators, see figure 56. The break sections between the undulators are

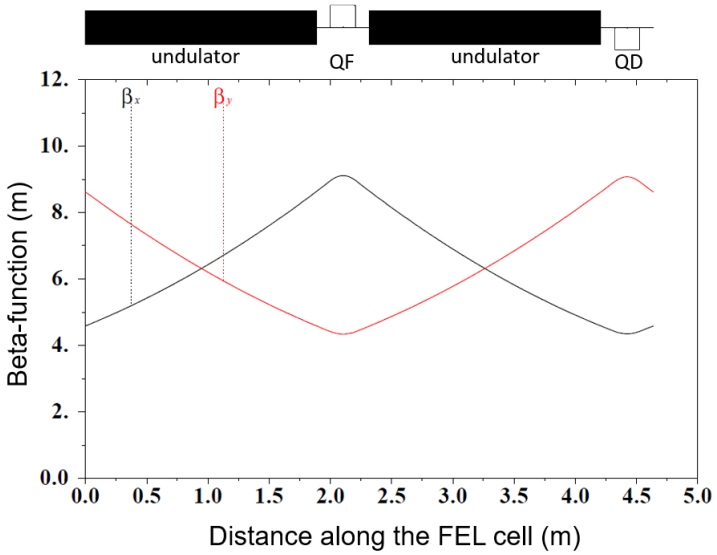

Figure 56. Undulator lattice cell. Black and red curves show horizontal and vertical beta-functions, respectively.

0.43 m-long and contain either focusing (QF) or defocusing (QD) 0.2 m-long quadrupoles. Overall, eight identical cells and sixteen undulators are used.

Figure 57 shows the growth of the peak X-ray power produced in the XFEL in two cases: (i) with undulators tuned to have $K = 1$ and (ii) to have $K = 1.57$. The X-ray peak power at the gain saturation and the lengths of the undulator line required to reach the gain saturation are shown in table 10. Two numbers in brackets show peak power calculated using the empirical formula given by eq. (17) in [116].

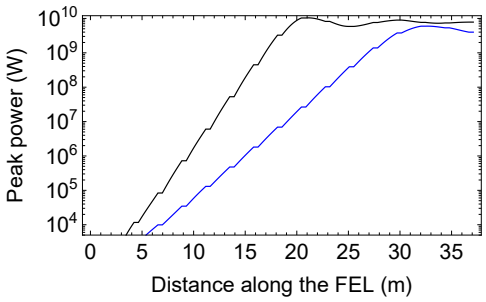

Figure 57. X-ray peak power versus the distance along the XFEL. The case of 10.2 keV photon energy is shown in blue color, and the case of the 7.6 keV photon energy is shown in black color.

Table 10. XFEL parameters.

Parameter	7.6 keV	10.2 keV	Unit
X-ray peak power	10.4(12.3)	6.0(7.0)	GW
X-ray pulse duration	≤33	≤33	fs
Saturation length	21.1	32.7	m

It is important to note that the peak XFEL power can be further increased through the use of current-enhanced self-amplified spontaneous emission (ESASE) [117] and unudulator tapering [118].

However, implementing ESASE would require performing laser-assisted energy modulation of the electron beam before it enters the undulator using a high repetition rate laser. As such, we leave a detailed analysis of this option for future investigations.

7 Conclusion

In this review, the focus has been on a description of the design, fabrication, and testing of the principal components of a compact corrugated waveguide-based collinear wakefield accelerator module. These components were manufactured by various vendors with dimensional tolerances incorporated into their design and were shown to be suitable for usage as-is in an actual fully functional accelerator. Thermal and structural analyses were performed, confirming accelerator suitability for operation at frequencies on the order of tens of kilohertz. To the best of our knowledge, the A-STAR collinear wakefield accelerator is unique among novel compact accelerator concepts due to its ability to support the high repetition rate for XFEL operation essential for photon-hungry experimental techniques such as coherent and incoherent diffractive imaging. The sub-THz frequency has been selected for the accelerating wakefield mode to enhance the attenuation of the field in the corrugated structure and to yield a nanosecond duration electromagnetic pulse in anticipation of achieving a high threshold for the electrical breakdown.

It has been shown that the beam breakup instability sets an upper limit on the maximum accelerating field in A-STAR, which is common to all structure-based collinear wakefield accelerators. It was also noted, however, that the trade-off between obtaining the high accelerating field and high-energy electrons leads to the selection of the same maximum field as defined by the beam breakup instability.

The stable deceleration of the drive bunch to low energies assisted by the quadrupole wiggler boosts the accelerator wall-plug efficiency and the witness bunch energy. Several full-sized quadrupoles were fabricated and equipped with knobs for precision mechanical tuning of the quadrupole's magnetic center, yaw, and pitch rotations. A sub-micrometer accuracy in the alignment of these quadrupoles assembled to represent several wiggler periods was demonstrated.

Representing a breakthrough in undulator technology, a concept of a small gap, small size undulator with an adjustable undulator parameter was developed and validated through the fabrication and characterization of an undulator using a legacy magnetic structure.

The research described in this review represents a new milestone in the ongoing design study of a compact, multiuser, high pulse repetition rate XFEL facility.

Acknowledgments

This manuscript is based upon work supported by Laboratory Directed Research and Development (LDRD) funding from Argonne National Laboratory (ANL), provided by the Director, Office of Science, of the U.S. Department of Energy under Contract No. DE-AC02-06CH11357. Useful discussions with G. Navrotski and J. Power from ANL, and W.-H. Tan from SLAC are gratefully acknowledged. A.Z is grateful to S. Reiche from the Paul Scherrer Institute and C. Hall from RadiaSoft for their invaluable assistance in performing calculations on the Sirepo server at RadiaSoft using the Genesis code. We are grateful to J. Byrd from ANL and S. Streiffer currently at Oak Ridge National Laboratory for their prolonged support of our work. We are grateful to J. Conway, N. Kuzmanovic, and W. Toter from the central shop in the ANL and B. Bentley, K. Pearson, and C. Redding from

2025 JINST 20 P01023

the central shop in the Lawrence Berkeley National Laboratory for the high-quality fabrication of the accelerator components. We thank the Accelerator Test Facility staff at Brookhaven National Laboratory for their support during the experiments.

A Abbreviations and symbols

Table 11. List of abbreviations.

Abbreviation	Definition
A-STAR	Argonne's Sub-Terahertz Accelerator
ATF	Accelerator Test Facility
BBU	beam breakup instability
BNS	Balakin-Novokhatsky-Smirnov damping
BW	bandwidth
CLIC	Compact Linear Collider
CVD	chemical vapor deposition
CWA	collinear wakefield accelerator
CWG	corrugated waveguide
DBA	drive bunch accelerator
DUT	device under the test
EDM	electrical discharge machining
EM	electromagnetic
FNAPU	force-neutral adjustable phase undulator
HOM	high order modes
ID	internal diameter
IOM	integrated offset monitor
OD	outside diameter
PM	permanent magnet
R&D	research and development
RF	radio frequency
SWFA	structure-based wakefield accelerator
SRF	superconducting radio frequency
TPX	polymethylpentene
TS	transition section
XFEL	X-ray free-electron laser

Table 12. List of variables.

Variable	Definition
a	minor radius of the CWG
$\hat{a}$	a/λ
α	attenuation constant

Variable	Definition
B	relative laser-induced energy modulation amplitude
B_{q}	pole tip magnetic field
β_g	v_g/c
c	speed of light
d	corrugation depth
$\Delta\mathcal{E}$	laser-induced energy modulation amplitude
ΔT	transient temperature rise
Δt	duration of the radiation pulse
Δx	horizontal offset
E	wakefield
E_{acc}	peak accelerating field
E_{dec}	peak decelerating field
E_{max}	peak surface electric field
$\mathcal{E}$	beam energy
$\hat{\mathcal{E}}$	energy of reference particle
ϵ	relative permittivity
ϵ_{nx}	normalized horizontal emittance
$F_\perp$	Lorentz force
f_m	monopole mode frequency
f_d	dipole mode frequency
f_r	bunch repetition rate
ϕ	phase advance per corrugation cell
ϕ_{RF}	linac RF phase
G	Green's function
G_{eff}	effective quadrupole field gradient
G_{max}	maximum quadrupole field gradient
g	corrugation gap width
γ	relativistic factor
H_{max}	peak surface magnetic field
k	wave vector
k_1	wave vector of dipole mode
K	undulator parameter
$\kappa_\parallel$	loss factor
$\kappa_\perp$	kick factor
ξ	$(g-t)/p$
ℓ_b	bunch length
λ	wavelength of the TM_{01} synchronous mode
L	length of the "doorstep" distribution
L_{acc}	accelerator module length
L_{c}	corrugated waveguide length
L_{eff}	effective quadrupole length
L_{q}	quadrupole length

2025 JINST 20 P01023

Variable	Definition
λ_L	laser wavelength
p	corrugation period
P	instantaneous RF pulse power
P_{diss}	power dissipation per module
q	charge distribution
q_0	drive bunch charge
Q_{diss}	energy dissipation distribution
r_t	corrugation tooth radius
r_g	corrugation vacuum gap floor radius
$\mathcal{R}$	transformer ratio
Rz, Rx, Ry	roll, pitch and yaw rotations
Ra	surface roughness parameter
S_{11}	RF back reflection coefficient
S_{21}	RF transmission loss coefficient
σ	electrical conductivity
$\sigma_{\mathcal{E}\text{w}}$	witness bunch energy spread
t	corrugation tooth width
τ	RF pulse decay time constant
θ	step function
v	electron bunch velocity
v_g	group velocity
W_{diss}	average thermal power density
z	distance from the bunch head

References

[1] J.C. Hemminger et al., *Challenges at the Frontiers of Matter and Energy: Transformative Opportunities for Discovery Science*, U.S. Department of Energy Office of Scientific and Technical Information, Oak Ridge, TN, U.S.A. (2015) [DOI:10.2172/1283188].

[2] C. Bostedt et al., *Linac Coherent Light Source: The first five years*, *Rev. Mod. Phys.* **88** (2016) 015007.

[3] C. Pellegrini, *X-ray free-electron lasers: from dreams to reality*, *Phys. Scr.* **2016** (2016) 014004.

[4] W. Ackermann, G. Asova, V. Ayvazyan et al., *Operation of a free-electron laser from the extreme ultraviolet to the water window*, *Nat. Photonics* **1** (2007) 336.

[5] P. Emma, R. Akre, J. Arthur et al., *First lasing and operation of an ångstrom-wavelength free-electron laser*, *Nat. Photonics* **4** (2010) 641.

[6] T. Ishikawa, H. Aoyagi, T. Asano et al., *A compact X-ray free-electron laser emitting in the sub-ångström region*, *Nat. Photonics* **6** (2012) 540.

[7] E. Allaria, R. Appio, L. Badano et al., *Highly coherent and stable pulses from the FERMI seeded free-electron laser in the extreme ultraviolet*, *Nat. Photonics* **6** (2012) 699.

[8] H.-S. Kang, C.-K. Min, H. Heo et al., *Hard X-ray free-electron laser with femtosecond-scale timing jitter*, *Nat. Photonics* **11** (2017) 708.

2025 JINST 20 P01023

[9] W. Decking, S. Abeghyan, P. Abramian et al., *A MHz-repetition-rate hard X-ray free-electron laser driven by a superconducting linear accelerator*, *Nat. Photonics* **14** (2020) 391.

[10] E. Prat, R. Abela, M. Aiba et al., *A compact and cost-effective hard x-ray free-electron laser driven by a high-brightness and low-energy electron beam*, *Nat. Photonics* **14** (2020) 748.

[11] B. Liu et al., *The SXFEL Upgrade: From Test Facility to User Facility*, *Appl. Sci.* **12** (2022) 176.

[12] LCLS-II Design Study Group, *LCLS-II final design report*, LCLSII-1.1-DR-0251-R0 (2015).

[13] R. Brinkmann, E.A. Schneidmiller, J. Sekutowicz and M.V. Yurkov, *Prospects for CW and LP operation of the European XFEL in hard X-ray regime*, *Nucl. Instrum. Meth. A* **768** (2014) 20 [arXiv:1403.0465].

[14] T. Raubenheimer, *The LCLS-II-HE, A High Energy Upgrade of the LCLS-II*, in the proceedings of the *60th ICFA Advanced Beam Dynamics Workshop on Future Light Sources (FLS2018)*, Shanghai, China, 5–9 March 2018, JACoW Publishing, Geneva, Switzerland (2018) [DOI:10.18429/JACoW-FLS2018-MOP1WA02].

[15] Z. Zhao, *XFEL Projects in China*, in the proceedings of the *29th Linear Accelerator Conference*, Beijing, China, 16–21 September 2018.

[16] Z. Zhao, D. Wang, Z.-H. Yang and L. Yin, *SCLF: An 8 GeV CW SCRF Linac-Based X-Ray FEL Facility in Shanghai*, in the proceedings of the *38th International Free-Electron Laser Conference (FEL 2017)*, Santa Fe, U.S.A., 20–25 August 2017, JACoW Publishing, Geneva, Switzerland (2018), pp. 182–184 [DOI:10.18429/JACoW-FEL2017-MOP055].

[17] L. Serafini, A. Bacci, A. Bellandi et al., *MariX, an advanced MHz-class repetition rate X-ray source for linear regime time-resolved spectroscopy and photon scattering*, *Nucl. Instrum. Meth. A* **930** (2019) 167.

[18] D. Dunning et al., *An introduction to the U.K. XFEL conceptual design and options analysis*, in the proceedings of the *14th International Particle Accelerator Conference (IPAC'23)*, Venice, Italy, 7–12 May 2023, JACoW Publishing, Geneva, Switzerland (2023), pp. 1909–1912 [DOI:10.18429/JACoW-IPAC2023-TUPL071].

[19] R. Neutze, R. Wouts, D. van der Spoel et al., *Potential for biomolecular imaging with femtosecond X-ray pulses*, *Nature* **406** (2000) 752.

[20] H. Chapman, A. Barty, M. Bogan et al., *Femtosecond diffractive imaging with a soft-X-ray free-electron laser*, *Nat. Phys.* **2** (2006) 839 [physics/0610044].

[21] A. Classen, K. Ayyer, H.N. Chapman, R. Röhlsberger and J. von Zanthier, *Incoherent Diffractive Imaging via Intensity Correlations of Hard X Rays*, *Phys. Rev. Lett.* **119** (2017) 053401.

[22] P.J. Ho, C. Knight and L. Young, *Fluorescence intensity correlation imaging with high spatial resolution and elemental contrast using intense x-ray pulses*, *Struct. Dyn.* **8** (2021) 044101.

[23] A. Schropp and C.G. Schroer, *Dose requirements for resolving a given feature in an object by coherent x-ray diffraction imaging*, *New J. Phys.* **12** (2010) 035016.

[24] P.J. Ho, C. Knight, M. Tegze, G. Faigel, C. Bostedt and L. Young, *Atomistic three-dimensional coherent x-ray imaging of nonbiological systems*, *Phys. Rev. A* **94** (2016) 063823.

[25] F. Trost et al., *Imaging via Correlation of X-Ray Fluorescence Photons*, *Phys. Rev. Lett.* **130** (2023) 173201.

[26] P.J. Ho, private information.

[27] J.-P. Delahaye et al., *A Beam Driven Plasma-wakefield Linear Collider from Higgs Factory to Multi-TeV*, in the proceedings of the *5th International Particle Accelerator Conference*, Dresden, Germany, 16 June 2013–20 June 2014, JACoW Publishing, Geneva, Switzerland (2014), pp. 3791–3793 [DOI:10.18429/JACoW-IPAC2014-THPRI013].

2025 JINST 20 P01023

[28] C.B. Schroeder, E. Esarey, C.G.R. Geddes, C. Benedetti and W.P. Leemans, *Physics considerations for laser-plasma linear colliders*, *Phys. Rev. Spec. Top. Accel. Beams* **13** (2010) 101301.

[29] C. Jing, *Dielectric Wakefield Accelerators*, *Rev. Accel Sci. Technol.* **09** (2016) 127.

[30] R.J. England, R.J. Noble, Z. Wu and M. Qi, *Dielectric Laser Acceleration*, *Rev. Mod. Phys.* **86** (2014) 1337 [arXiv:1309.7637].

[31] C. Adolphsen et al., *European Strategy for Particle Physics — Accelerator R & D Roadmap*, in *CERN Yellow Reports: Monographs* **1**, CERN, Geneva, Switzerland (2022) [DOI:10.23731/CYRM-2022-001] [arXiv:2201.07895].

[32] Z. Huang, Y. Ding and C.B. Schroeder, *Compact X-ray Free-Electron Laser from a Laser-Plasma Accelerator Using a Transverse-Gradient Undulator*, *Phys. Rev. Lett.* **109** (2012) 204801.

[33] A.R. Maier, A. Meseck, S. Reiche, C.B. Schroeder, T. Seggebrock and F. Grüner, *Demonstration Scheme for a Laser-Plasma-Driven Free-Electron Laser*, *Phys. Rev. X* **2** (2012) 031019.

[34] M.E. Couprie, M. Labat, C. Evain et al., *An application of laser-plasma acceleration: towards a free-electron laser amplification*, *Plasma Phys. Contr. Fusion* **58** (2016) 034020.

[35] M. Ferrario et al., *EuPRAXIA@SPARC_LAB Design study towards a compact FEL facility at LNF*, *Nucl. Instrum. Meth. A* **909** (2018) 134 [arXiv:1801.08717].

[36] R.W. Assmann et al., *EuPRAXIA Conceptual Design Report*, *Eur. Phys. J. Spec. Top.* **229** (2020) 3675.

[37] C. Emma, J. van Tilborg, R. Assmann et al., *Free electron lasers driven by plasma accelerators: status and near-term prospects*, *High Power Laser Sci. Eng.* **9** (2021) e57.

[38] W. Wang, K. Feng, L. Ke et al., *Free-electron lasing at* 27 *nanometres based on a laser wakefield accelerator*, *Nature* **595** (2021) 516.

[39] K. Feng, W. Wang and R. Li, *Development of Table-Top Free Electron Lasers Based on a Laser Wakefield Accelerator*, in *Progress in Ultrafast Intense Laser Science XVII*, *Topics in Applied Physics* **151**, K. Yamanouchi, L.F. DiMauro and W.T. Hill III eds., Springer, Cham, Switzerland (2024), pp. 197–210 [DOI:10.1007/978-3-031-55463-6_9].

[40] M. Galletti et al., *Prospects for free-electron lasers powered by plasma-wakefield-accelerated beams*, *Nat. Photonics* **18** (2024) 780.

[41] M. Bai et al., *C^3: A "Cool" Route to the Higgs Boson and Beyond*, in the proceedings of the *Snowmass 2021*, Seattle, WA, U.S.A., 17–26 July 2022, arXiv:2110.15800.

[42] E.A. Nanni et al., *Status and future plans for C^3 R&D*, 2023 *JINST* **18** P09040.

[43] J.B. Rosenzweig, N. Majernik, R.R. Robles et al., *An ultra-compact x-ray free-electron laser*, *New J. Phys.* **22** (2020) 093067 [arXiv:2003.06083].

[44] R.R. Robles, O. Camacho, A. Fukasawa, N. Majernik and J.B. Rosenzweig, *Versatile, High Brightness, Cryogenic Photoinjector Electron Source*, *Phys. Rev. Accel. Beams* **24** (2021) 063401 [arXiv:2103.08789].

[45] G. D'Auria et al., *The CompactLight Design Study*, *Eur. Phys. J. Spec. Top.* **233** (2024) 1.

[46] G.A. Voss and T. Weiland, *The wake field acceleration mechanism*, DESY-82-074 (1982).

[47] R.J. Briggs, T.J. Fessenden and V.K. Neil, *Electron autoacceleration*, in the proceedings of the *9th International Conference on the High-Energy Accelerators*, Stanford, CA, U.S.A., 2–7 May 1974, SLAC-R-839, A.E.C., Washington, D.C., U.S.A. (1975), pp. 278–282, https://slac.stanford.edu/pubs/slacreports/reports16/slac-r-839-b.pdf.

[48] M. Friedman, *Autoacceleration of an Intense Relativistic Electron Beam*, *Phys. Rev. Lett.* **31** (1973) 1107.

2025 JINST 20 P01023

[49] E.A. Perevedentsev and A.N. Skrinsky, *On the Use of the Intense Beams of Large Proton Accelerators to Excite the Accelerating Structure of a Linear Accelerator*, in the proceedings of the *6th All-Union Conference Charged Particle Accelerators, Dubna (Institute of Nuclear Physics*, Dubna, USSR, 11–13 October 1978, p. 272.

[50] Y. Chin, *The Wake Field Acceleration Using a Cavity of Elliptical Cross Section*, in the proceedings of the *12th International Linear Accelerator Conference (LINAC84)*, Darmstadt, Germany, 7–11 May 1984, pp. 159–161, https://accelconf.web.cern.ch/l84/papers/tup0026.pdf.

[51] W. Gai et al., *Experimental Demonstration of Wake Field Effects in Dielectric Structures*, *Phys. Rev. Lett.* **61** (1988) 2756.

[52] X. Lu et al., *Advanced RF Structures for Wakefield Acceleration and High-Gradient Research*, in the proceedings of the *Snowmass 2021*, Seattle, WA, U.S.A., 17–26 July 2022, arXiv:2203.08374.

[53] O. Brunner et al., *The CLIC project*, arXiv:2203.09186.

[54] I. Syratchev, D. Schulte, E. Adli and M. Taborelli, *High RF power production for CLIC*, in the proceedings of the *2007 IEEE Particle Accelerator Conference (PAC)*, Albuquerque, NM, U.S.A., 25–29 June 2007, IEEE (2007), pp. 2194–2196 [*Conf. Proc. C* **070625** (2007) 2194], https://accelconf.web.cern.ch/p07/PAPERS/WEPMN071.PDF.

[55] CLICdp and CLIC collaborations, *The Compact Linear Collider (CLIC) — 2018 Summary Report*, in *CERN Yellow Reports: Monographs* **2**, CERN, Geneva, Switzerland (2018), arXiv:1812.06018 [DOI:10.23731/CYRM-2018-002].

[56] K.L.F. Bane, P. Chen and P.B. Wilson, *On collinear wake field acceleration*, in the proceedings of the *11th Particle Accelerator Conference: Accelerator Engineering and Technology (PAC1985)*, Vancouver, BC, Canada, 13–16 May 1985, *IEEE Trans. Nucl. Sci.* **32** (1985) 3524.

[57] A. Grudiev, S. Calatroni and W. Wuensch, *New local field quantity describing the high gradient limit of accelerating structures*, *Phys. Rev. Spec. Top. Accel. Beams* **12** (2009) 102001 [*Erratum ibid.* **14** (2011) 099902].

[58] S.A. Barengolts et al., *Mechanism of vacuum breakdown in radio-frequency accelerating structures*, *Phys. Rev. Accel. Beams* **21** (2018) 061004.

[59] A. Zholents et al., *A preliminary design of the collinear dielectric wakefield accelerator*, *Nucl. Instrum. Meth. A* **829** (2016) 190.

[60] A. Zholents et al., *A Conceptual Design of a Compact Wakefield Accelerator for a High Repetition Rate Multi User X-ray Free-Electron Laser Facility*, in the proceedings of the *9th International Particle Accelerator Conference (IPAC'18)*, Vancouver, BC, Canada, 29 April–4 May 2018, JACoW Publishing, Geneva, Switzerland (2018), pp. 1266–1268 [DOI:10.18429/JACoW-IPAC2018-TUPMF010].

[61] J.Z. Xu, M. Qian and A. Zholents, *A force-neutral adjustable phase undulator for a compact x-ray FEL*, in the proceedings of the *14th International Particle Accelerator Conference (IPAC'23)*, Venice, Italy, 7–12 May 2023, JACoW Publishing, Geneva, Switzerland (2023), p. 1754 [DOI:10.1088/1742-6596/2687/3/032017].

[62] J. Xu, M. Qian and Y. Piao, *Force-neutral adjustable phase undulator*, in the proceedings of the *15th International Particle Accelerator Conference*, Nashville, TN, U.S.A., 19–24 May 2024, JACoW Publishing, Geneva, Switzerland (2024), pp. 1351–1354 [DOI:10.18429/JACoW-IPAC2024-TUPG5].

[63] W.-H. Tan, P. Piot and A. Zholents, *Formation of Temporally Shaped Electron Bunches for Beam-Driven Collinear Wakefield Accelerators*, *Phys. Rev. Accel. Beams* **24** (2021) 051303 [arXiv:2101.07414].

[64] S.S. Baturin and A. Zholents, *Upper limit for the accelerating gradient in the collinear wakefield accelerator as a function of the transformer ratio*, *Phys. Rev. Accel. Beams* **20** (2017) 061302.

2025 JINST 20 P01023

[65] B.W. Zotter and S.A. Kheifets, *Impedances and wakes in high-energy particle accelerators*, World Scientific (1998) [DOI:10.1142/3068].

[66] A. Chao, *Physics of Collective Beam Instabilities in High Energy Accelerators*, Wiley and Sons, New York, NY, U.S.A. (1993).

[67] A. Polyanin and A. Manzhirov, *Handbook of Integral Equations*, CRC Press, Boca Raton, FL, U.S.A. (1998).

[68] K.L.F. Bane, *Wakefields of Sub-Picosecond Electron Bunches*, SLAC-PUB-11829, SLAC, Stanford, CA, U.S.A. (2006).

[69] K.L.F. Bane and G. Stupakov, *Corrugated Pipe as a Beam Dechirper*, *Nucl. Instrum. Meth. A* **690** (2012) 106.

[70] S.S. Baturin and A.D. Kanareykin, *Cherenkov Radiation from Short Relativistic Bunches: General Approach*, *Phys. Rev. Lett.* **113** (2014) 214801 [arXiv:1308.6228].

[71] K.L.F. Bane and A.V. Novokhatskii, *The Resonator impedance model of surface roughness applied to the LCLS parameters*, SLAC-AP-117, SLAC, Stanford, CA, U.S.A. (1999).

[72] W.K.H. Panofsky and M. Bander, *Asymptotic Theory of Beam Break-Up in Linear Accelerators*, *Rev. Sci. Instrum.* **39** (1968) 206.

[73] V.K. Neil, L.S. Hall and R.K. Cooper, *Further Theoretical Studies Of The Beam Breakup Instability*, *Part. Accel.* **9** (1979) 213.

[74] A.W. Chao, B. Richter and C.-Y. Yao, *Beam Emittance Growth Caused by Transverse Deflecting Fields in a Linear Accelerator*, *Nucl. Instrum. Meth.* **178** (1980) 1.

[75] V.E. Balakin, A.V. Novokhatsky and V.P. Smirnov, *VLEPP: Transverse Beam Dynamics*, in the proceedings of the *12th International Conference on High-Energy Accelerators, HEACC 1983*, Fermilab, Batavia, IL, U.S.A., 11–16 August 1983, *Conf. Proc. C* **830811** (1983) 119.

[76] C. Li, W. Gai, C. Jing, J.G. Power, C.X. Tang and A. Zholents, *High gradient limits due to single bunch beam breakup in a collinear dielectric wakefield accelerator*, *Phys. Rev. Spec. Top. Accel. Beams* **17** (2014) 091302.

[77] D.Y. Shchegolkov, E.I. Simakov and A. Zholents, *Towards a Practical Multi-Meter Long Dielectric Wakefield Accelerator: Problems and Solutions*, *IEEE Trans. Nucl. Sci.* **63** (2016) 804.

[78] S.S. Baturin and A. Zholents, *Stability condition for the drive bunch in a collinear wakefield accelerator*, *Phys. Rev. Accel. Beams* **21** (2018) 031301 [arXiv:1709.08583].

[79] CST Microwave Studio, *Dassault Systems, Inc.*, (2020), https://www.cst.com/products/cstmws.

[80] A. Siy, N. Behdad, J. Booske, G. Waldschmidt and A. Zholents, *Design of a cylindrical corrugated waveguide for a collinear wakefield accelerator*, *Phys. Rev. Accel. Beams* **25** (2022) 121601.

[81] M. Dal Forno et al., *rf breakdown tests of mm-wave metallic accelerating structures*, *Phys. Rev. Accel. Beams* **19** (2016) 011301.

[82] D.P. Pritzkau and R.H. Siemann, *Experimental study of RF pulsed heating on oxygen free electronic copper*, *Phys. Rev. Spec. Top. Accel. Beams* **5** (2002) 112002.

[83] V. Dolgashev, S. Tantawi, Y. Higashi and B. Spataro, *Geometric dependence of radio-frequency breakdown in normal conducting accelerating structures*, *Appl. Phys. Lett.* **97** (2010) 171501.

[84] K. Suthar et al., *Determination of Maximum Repetition Rate of a Corrugated-Waveguide-Based Wakefield Accelerator*, in the proceedings of the *11th Mechanical Engineering Design of Synchrotron Radiation Equipment and Instrumentation (MEDSI 2020)*, Chicago, IL, U.S.A., 26–29 July 2021, JACoW Publishing, Geneva, Switzerland (2020), pp. 336–340 [DOI:10.18429/JACoW-MEDSI2020-THIO02].

2025 JINST 20 P01023

[85] Comsol Multiphysics, *COMSOL Multiphysics*, (2020), https://www.comsol.com/.

[86] X.F. Zhan, Q.D. Cao, K. Trieu and X.P. Zhang, *Microstructure and Mechanical Properties of Copper Microtubes Fabricated via the Electroforming Process*, *J. Mater. Eng. Perform.* **29** (2020) 1741.

[87] Q. Liao, L.-Q. Zhu, H.-C. Liu and W.-P. Li, *Mechanical properties of electroformed copper layers with gradient microstructure*, *Int. J. Miner. Metall. Mater.* **17** (2010) 69.

[88] E.O. Hall, *The Deformation and Ageing of Mild Steel: III Discussion of Results*, *Proc. Phys. Soc. Lond. B* **64** (1951) 747.

[89] N.J. Petch, *The Cleavage Strength of Polycrystals*, *J. Iron Steel Inst.* **174** (1953) 25.

[90] J.W. Dini and D.D. Snyder, *Electrodeposition of copper*, in *Modern Electroplating*, John Wiley and Sons, Ltd. (2010), pp. 33–78 [DOI:10.1002/9780470602638.ch2].

[91] A. Siy et al., *Fabrication and testing of corrugated waveguides for a collinear wakefield accelerator*, *Phys. Rev. Accel. Beams* **25** (2022) 021302.

[92] P. Fallah, L.A. Hof and R. Wuthrich, *Fabrication of high-thickness and low surface roughness metal parts by a hybrid electrochemical manufacturing process*, *Adv. Ind. Manuf. Eng.* **2** (2021) 100034.

[93] K. Suthar, E. Trakhtenberg, S. Sorsher and A. Zholents, *Vacuum Analysis of a Corrugated Waveguide Wakefield Accelerator*, in the proceedings of the *11th Mechanical Engineering Design of Synchrotron Radiation Equipment and Instrumentation*, Chicago, IL, U.S.A., 26–29 July 2021, p. 160 [DOI:10.18429/JACoW-MEDSI2020-TUPB07].

[94] T. Abe et al., *Outgassing rate of highly pure copper electroplating applied to RF cavities*, in the proceedings of the *10th European Particle Accelerator Conference (EPAC 06)*, Edinburgh, U.K., 26–30 June 2006, *Conf. Proc. C* **060626** (2006) 1307.

[95] P. Massuti Ballester, *Outgassing Analysis of different Copper Materials for Ultra-High Vacuum by Thermal Desorption Spectroscopy*, Ph.D. Thesis, Saarland University, Saarbrücken, Germany (2017).

[96] N. Kirby, M. Berry, I. Blumenfeld, M. Hogan, R. Ischebeck and R. Siemann, *Emittance Growth from Multiple Coulomb Scattering in a Plasma Wakefield Accelerator*, in the proceedings of the *2007 IEEE Particle Accelerator Conference (PAC)*, Albuquerque, NM, U.S.A., 25–29 June 2007, pp. 3097–3099 [*Conf. Proc. C* **070625** (2007) 3097].

[97] A. Siy, N. Behdad, J. Booske, G. Waldschmidt and A. Zholents, *Electromagnetic design of the transition section between modules of a wakefield accelerator*, *Phys. Rev. Accel. Beams* **26** (2023) 012802.

[98] G. Gantenbein et al., *First Operation of a Step-Frequency Tunable* 1 *MW Gyrotron With a Diamond Brewster Angle Output Window*, *IEEE Trans. Electron Devices* **61** (2014) 1806.

[99] Y.A. Gorelov et al., *Characteristics of diamond windows on the* 1 *MW,* 110 *GHz gyrotron systems on the DIII-D tokamak*, in the proceedings of the *Twenty Seventh International Conference on Infrared and Millimeter Waves*, San Diego, CA, U.S.A., 26 September 2002, pp. 161–162 [DOI:10.1109/icimw.2002.1076134].

[100] B. Popovic et al., *Design of Miniature Waveguides and Diamond Window Assembly for RF Extraction and Vacuum Isolation for the CWA*, in the proceedings of the *11th Mechanical Engineering Design of Synchrotron Radiation Equipment and Instrumentation (MEDSI 2020)*, Chicago, IL, U.S.A., 26–29 July 2021, JACoW Publishing, Geneva, Switzerland (2021), pp. 336–340 [DOI:10.18429/JACoW-MEDSI2020-TUPB06].

[101] S. Lee et al., *Design and Fabrication Challenges of Transition Section for the CWA Module*, in the proceedings of the *11th Mechanical Engineering Design of Synchrotron Radiation Equipment and Instrumentation (MEDSI 2020)*, Chicago, IL, U.S.A., 26–29 July 2021, JACoW Publishing, Geneva, Switzerland (2021), pp. 273–275 [DOI:10.18429/JACoW-MEDSI2020-WEPB04].

2025 JINST 20 P01023

[102] A. Zholents et al., *Fabrication and testing of the transition section between modules of a wakefield accelerator*, *Phys. Rev. Accel. Beams* **27** (2024) 081303.

[103] M. Qian et al., *Quadrupole wiggler for a collinear wakefield accelerator*, *Phys. Rev. Accel. Beams* **28** (2025) 012401.

[104] Opera 3D, https://www.3ds.com/products/simulia/opera.

[105] ATF, https://www.bnl.gov/atf.

[106] V. Yakimenko, *The Accelerator Test Facility at Brookhaven: Main capabilities*, *AIP Conf. Proc.* **737** (2004) 677.

[107] K.L.F. Bane et al., *Measurements of Terahertz Radiation Generated using a Metallic, Corrugated Pipe*, *Nucl. Instrum. Meth. A* **844** (2017) 121 [arXiv:1608.06337].

[108] S. Antipov et al., *Efficient extraction of high power THz radiation generated by an ultra-relativistic electron beam in a dielectric loaded waveguide*, *Appl. Phys. Lett.* **109** (2016) 142901.

[109] R.W. Warren, *Limitations on the use of the pulsed-wire field measuring technique*, *Nucl. Instrum. Meth. A* **272** (1988) 257.

[110] Z. Wolf, *A vibrating wire system for quadrupole fiducialization*, LCLS-TN-05-11, Stanford Linear Accelerator Center, Menlo Park, CA, U.S.A. (2005).

[111] D. Arbelaez, T.M. Wilks, A. Madur, S.O. Prestemon, S. Marks and R.D. Schlueter, *A dispersion and pulse width correction algorithm for the pulsed wire method*, *Nucl. Instrum. Meth. A* **716** (2013) 62.

[112] M. Kasa and A. Zholents, *Pulsed Wire Measurements of a High Field Gradient Quadrupole Wiggler*, in the proceedings of the *9th International Particle Accelerator Conference (IPAC'18)*, Vancouver, BC, Canada, 29 April–4 May 2018, pp. 1257–1259 [DOI:10.18429/JACoW-IPAC2018-TUPMF006].

[113] S. Reiche, *GENESIS 1.3: A fully 3D time dependent FEL simulation code*, *Nucl. Instrum. Meth. A* **429** (1999) 243.

[114] M. Xie, *Exact and variational solutions of 3D eigenmodes in high gain FELs*, *Nucl. Instrum. Meth. A* **445** (2000) 59.

[115] E. Prat et al., *Generation and Characterization of Intense Ultralow-Emittance Electron Beams for Compact X-Ray Free-Electron Lasers*, *Phys. Rev. Lett.* **123** (2019) 234801.

[116] K.-J. Kim and M. Xie, *Self-amplified spontaneous emission for short wavelength coherent radiation*, *Nucl. Instrum. Meth. A* **331** (1993) 359.

[117] A. Zholents, *Method of an enhanced self-amplified spontaneous emission for x-ray free electron lasers*, *Phys. Rev. Spec. Top. Accel. Beams* **8** (2005) 040701.

[118] J. Duris, S. Li, E. Champenois, J. MacArthur et al., *Tunable Isolated Attosecond X-ray Pulses with Gigawatt Peak Power from a Free-Electron Laser*, *Nat. Photonics* **14** (2020) 30 [arXiv:1906.10649].

2025 JINST 20 P01023